metals

MDPI

*Review*

# Grain Boundary Wetting by the Second Solid Phase: 20 Years of History

**Boris Straumal [1,2,*], Tatiana Lepkova [2], Anna Korneva [3], Gregory Gerstein [4], Olga Kogtenkova [1] and Alena Gornakova [1]**

[1] Osipyan Institute of Solid State Physics, Russian Academy of Sciences, Ac. Osipyan Str. 2, 142432 Chernogolovka, Russia; kogtenkova@issp.ac.ru (O.K.); alenahas@issp.ac.ru (A.G.)
[2] Department of Physical Chemistry, National University of Science and Technology "MISIS", 119049 Moscow, Russia; lepkovatl@mail.ru
[3] Institute of Metallurgy and Materials Science, Polish Academy of Sciences, Reymonta St. 25, 30-059 Cracow, Poland; a.korniewa@imim.pl
[4] Institut für Werkstoffkunde (Materials Science), Leibniz Universität Hannover, An der Universität 2, 30823 Garbsen, Germany; gerstein@iw.uni-hannover.de
* Correspondence: straumal@issp.ac.ru; Tel.: +7-916-6768-673

**Abstract:** Grain boundaries (GBs) can be wetted by a second phase. This phase can be not only liquid (or melted), but it can also be solid. GB wetting can be incomplete (partial) or complete. In the case of incomplete (partial) wetting, the liquid forms in the GB droplets, and the second solid phase forms a chain of (usually lenticular) precipitates. Droplets or precipitates have a non-zero contact angle with the GB. In the case of complete GB wetting, the second phase (liquid or solid) forms in the GB continuous layers between matrix grains. These GB layers completely separate the matrix crystallites from each other. GB wetting by a second solid phase has some important differences from GB wetting by the melt phase. In the latter case, the contact angle always decreases with increasing temperature. If the wetting phase is solid, the contact angle can also increase with increasing temperature. Moreover, the transition from partial to complete wetting can be followed by the opposite transition from complete to partial GB wetting. The GB triple junctions are completely wetted in the broader temperature interval than GBs. Since Phase 2 is also solid, it contains GBs as well. This means that not only can Phase 2 wet the GBs in Phase 1, but the opposite can also occur when Phase 1 can wet the GBs in Phase 2. GB wetting by the second solid phase was observed in the Al-, Mg-, Co-, Ni-, Fe-, Cu-, Zr-, and Ti-based alloys as well as in multicomponent alloys, including high-entropy ones. It can seriously influence various properties of materials.

**Keywords:** grain boundaries; wetting; melt; solid phase; phase transitions; phase diagrams

check for updates

**Citation:** Straumal, B.; Lepkova, T.; Korneva, A.; Gerstein, G.; Kogtenkova, O.; Gornakova, A. Grain Boundary Wetting by the Second Solid Phase: 20 Years of History. *Metals* **2023**, *13*, 929. https://doi.org/10.3390/met13050929

Academic Editor: Xiao-Wu Li

Received: 17 March 2023
Revised: 30 April 2023
Accepted: 8 May 2023
Published: 10 May 2023

## 1. Introduction

The phenomenon of wetting of solid surfaces with liquids has been known for many centuries. The study of wetting metal or ceramic surfaces with melts has a shorter history. In reality, this issue began to be investigated shortly after the Second World War, when the technology of liquid-phase sintering of metal or ceramic powders was developed [1]. With incomplete (or partial) wetting of the free surface, a droplet of the liquid phase lies on a solid surface and forms a non-zero contact angle θ with it. Incomplete wetting occurs if $\sigma_{SG} < \sigma_{SL} + \sigma_{LG}$ where $\sigma_{SG}$ is the energy of the solid-gas interface, $\sigma_{sl}$ is the energy of the boundary between solid and liquid phases, and $\sigma_{lg}$ is the energy of the boundary between the liquid phase and gas. It follows from the conditions of mechanical equilibrium that $\sigma_{SG} = \sigma_{SL} + \sigma_{LG} \cos\theta$. If $\sigma_{SG} > \sigma_{SL} + \sigma_{LG}$, complete wetting occurs, the liquid spreads over the surface, and the contact angle between the liquid droplet and the solid substrate is formally equal to zero.

Almost simultaneously with the study of the wetting of the free surface of metals or ceramics by melts began the study of the grain boundary (GB) wetting by a liquid phase. This is not surprising since the goal of liquid-phase sintering is to form a product that is as compact and pore-free as possible. In this case, individual grains or solid crystallites approach each other. Naturally, the question immediately arises, what has to be the configuration of the melt between these crystallites? Namely, whether the melt forms continuous interlayers between grains (complete wetting) or whether chains of liquid inclusions or droplets appear (partial or incomplete GB wetting by the liquid phase). The condition for complete GB wetting by the liquid phase is $\sigma_{GB} > 2\sigma_{SL,}$ where $\sigma_{GB}$ is the grain boundary energy. The condition for incomplete (partial) wetting of the grain boundaries by the liquid phase is $\sigma_{GB} < 2\sigma_{SL}$.

Around the mid-1950s, it was discovered that when the temperature changes, the wetting conditions can also change. Namely, with an increase in temperature, a transition can occur from incomplete wetting of the surfaces or GBs by the melt to complete one. In this case, the temperature dependence of $\sigma_{GB}(T)$ and $2\sigma_{SL}(T)$ intersect at $T_{wGB}$. This is the temperature of the GB wetting phase transformation (Figure 1a).

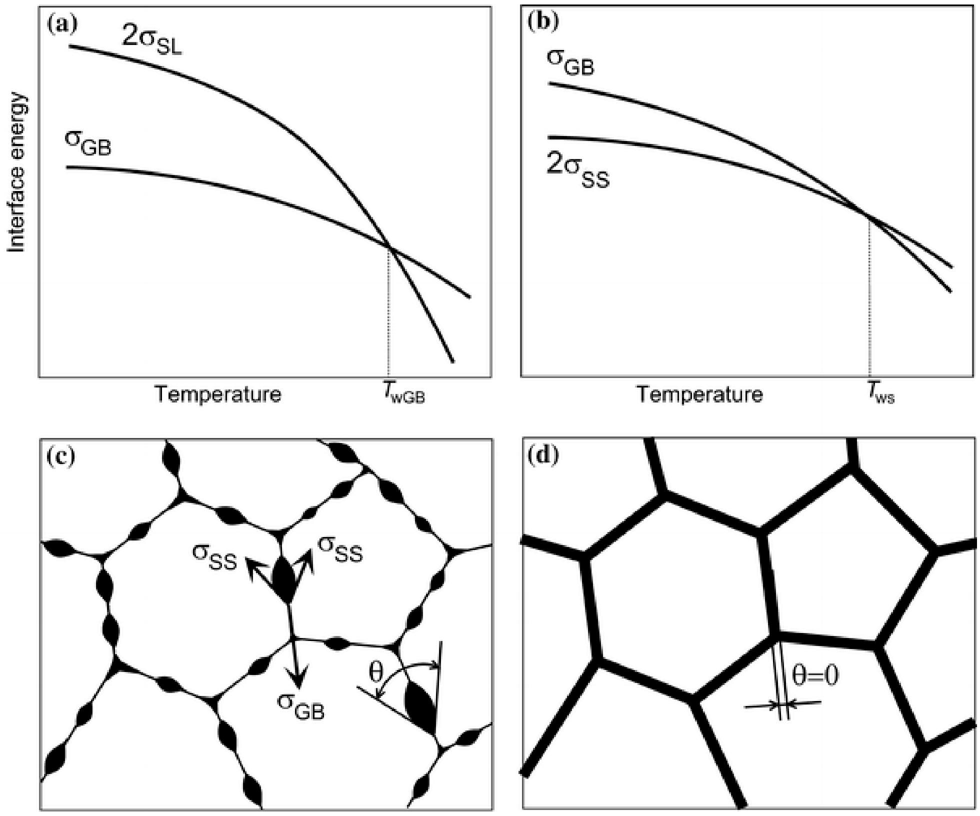

**Figure 1.** Schematic comparison of temperature dependence for GB energy $\sigma_{GB}$ and energy of two interphase boundaries with liquid $2\sigma_{SL}$ or solid $2\sigma_{SS}$ phases. (**a**) Phase transformation between incomplete and complete GB wetting with a melt at $T_{wGB}$. (**b**) Phase transformation between incomplete and complete GB wetting with another solid phase at $T_{ws}$. (**c**) Example of a polycrystal where the GBs are incompletely wetted by another solid phase. In this case, $\sigma_{GB} < 2\sigma_{SS}$ and the second solid phase has a shape of lenticular precipitates along GBs with the non-zero $\theta > 0$ contact angle. (**d**) Example of the polycrystal with GBs completely wetted by a second solid phase. In this case, $\sigma_{GB} > 2\sigma_{SS}$, the second solid phase has a shape of continuous rather thick layers along GBs with zero contact angle $\theta = 0$. Reprinted with permission from Ref. [2]. Copyright 2011 Springer.

Below $T_{wGB}$ $\sigma_{GB} < 2\sigma_{SL}$ and GBs are partially wetted by the liquid phase. Above $T_{wGB}$ $\sigma_{GB} < 2\sigma_{SL}$ and GBs are completely (fully) wetted by the melt. Cahn [3] and Ebner and Saam [4] analyzed the case of a liquid droplet on a solid surface by increasing temperature. They first supposed that, in this case, a transformation from partial to complete wetting could take place. They also demonstrated that it is a true surface phase transformation. Refs. [5–11] contain the early reviews of the publications about wetting phase transformation. Cahn's idea [3] initiated the experimental studies of GB wetting phase transformations. They were initially performed in Ag–Pb, Zn–Sn, and Zn–Sn–Pb polycrystals (see Ref. [12] and the references therein). GB wetting phase transformations can be first-order or second-order [13]. A detailed study of the physical foundations of such transformations became possible when the transitions from incomplete wetting to complete wetting began to be studied with bicrystals containing single-grain boundaries [14–16].

Several decades later, namely in the early 2000s, it was discovered that the second phase, which wets the grain boundaries, is not always liquid but can also be a solid [2,17]. From the point of view of thermodynamics, the conditions for wetting the boundaries with the second phase, if the second phase is solid, practically do not differ from the conditions for wetting with the melt, namely, the condition for complete wetting of the GBs by the second solid phase is $\sigma_{GB} > 2\sigma_{SS}$ where $2\sigma_{SS}$ is the energy of a boundary between two different solid phases. The condition for incomplete (partial) GB wetting by the other solid phase is $\sigma_{GB} < 2\sigma_{SS}$. In Figure 1, schemes for the polycrystals with GBs completely (Figure 1d) and partially (Figure 1c) wetted by a second solid phase are shown. Similar to GB wetting with a melt, the transition between complete and partial GB wetting can also proceed at a certain temperature $T_{ws}$. It is important to underline that for solid-solid wetting, the condition $\sigma_{GB} < 2\sigma_{SS}$ includes interfacial energy of the two solid phases $2\sigma_{SS}$. However, the $\sigma_{SS}$ value is affected by interfacial structure, e.g., a coherent interface should have smaller interfacial energy than an incoherent interface. This fact should also be considered in the discussion of GB wetting by other solid phases.

A natural question arises. Why was it possible to detect GB wetting by the second solid phase only half a century after the beginning of the study of GB wetting by the liquid phase? It is because of the slow kinetics of the wetting process with the second solid phase. If the second phase is liquid, then the equilibrium in the system, due to the high rate of mass transfer through the liquid, is established very quickly, literally within a few minutes, at least within half an hour. If both phases are solid, the mass transfer rate is many orders of magnitude lower than in a liquid. This means that it takes a much longer time to reach equilibrium. For example, in typical experiments on the study of GB wetting by the second solid phase, the duration of annealing is usually several hundred hours and can even reach several months. It becomes clear that the phenomenon of GB wetting by the second solid phase could not be discovered by chance. It required a purposeful search and understanding of the nature of the phenomenon.

Almost 20 years have passed since the discovery of the phenomenon of GB wetting by other solid phases in 2004 [17]. The indications of GB wetting by other solid phases were found and studied in a large circle of systems such as Al alloys [16–35], Fe-based alloys and steels [36–76], Co- and Ni-based alloys [77–85], Cu alloys [86–90], Ti- and Zr-based alloys [91–123], Mg alloys [124–131], as well multicomponent and high-entropy alloys [132–144] (more details see below, especially in Section 6). Some fundamental differences were also found between wetting by other solid phases and wetting by the liquid phase. Namely, if the wetting phase is solid, the contact angle can increase with increasing temperature. Moreover, the transition from partial to complete wetting can be followed by the opposite transition from complete to partial GB wetting. The GB triple junctions are completely wetted in the broader temperature interval than GBs. Since the wetting phase is also solid, it contains GBs as well. It means that not only can Phase 2 wet the GBs in Phase 1, but the opposite can also occur when Phase 1 wets the GBs in Phase 2.

## 2. Transition from Incomplete to Complete GB Wetting with Increasing Temperature

The transition from incomplete to complete wetting of grain boundaries occurs when the grain boundary energy $\sigma_{GB}$ becomes higher than the energy of two interphase boundaries. In the case of liquid-phase wetting, this is the energy of two interfaces between the solid and liquid phases $2\sigma_{SL}$. In the case of GB wetting by a second solid phase, this is the energy of two interfaces between the solid α- and solid β-phases $2\sigma_{SS}$. The free energy of grain and interphase boundaries always decreases with increasing temperature. If one of the phases is liquid, then its entropy is higher than that of a solid body, and the free energy of the interface between the liquid and solid phases $2\sigma_{SL}$, as a rule, decreases with increasing temperature faster than the free energy of the interface between two grains of the same phase $\sigma_{GB}$ (see the diagram in Figure 1a). This means that at each individual GB, the transition from incomplete wetting to complete wetting by the melt always occurs with increasing temperature. It concerns, however, only the thermodynamic issue (namely, how the ratio $\sigma_{GB}/2\sigma_{SS}$ or $\sigma_{GB}/2\sigma_{SL}$ changes with increasing temperature). Therefore, we should emphasize the difference between the thermodynamic and kinetic aspects of the GB wetting problem. The kinetics of equilibration is determined by the diffusion in the solid or liquid phases, and its rate always grows with increasing temperature.

If individual grain boundaries in bicrystals are not analyzed but instead a whole ensemble of GBs in a polycrystal at once, then each individual GB has its own value of $T_{wGB}$. As a result, the fraction of fully wetted GBs increases with increasing temperature, and the fraction of partially wetted GBs decreases. In the case of GB wetting by the second solid phase, the situation in many systems is similar to liquid-phase wetting. In other words, the fraction of completely wetted GBs also increases with increasing temperature until it reaches 100%. Then all GBs in the α phase will be separated from each other by the layers of the β phase.

The first work where GB wetting by other solid phases was intentionally studied was published in 2004 [17]. It considered an aluminum-zinc system, or rather, the trapezoidal part of the Al−Zn phase diagram. It is between the temperature of the eutectic transformation of the melt into a mixture of solid phases (Al) + (Zn) at 381 °C and the temperature of monotectoid decomposition of the Al-based solid solution (Al) at 277 °C. At 277 °C, (Al) decomposes into two solid solutions (Al)′ and (Al)″. The (Al)″ phase is enriched in zinc, and the (Al)′ phase is depleted in zinc. Figure 2 shows the microstructure of this alloy in the cast state before prolonged annealing [17]. It consists of typical eutectic grains where the plates of an aluminum-rich phase and a zinc-rich phase alternate. Moreover, it is clearly seen that when the cast alloy is cooled, the aluminum-rich phase undergoes a monotectoid transformation and, in turn, decomposes into two phases, one rich in aluminum (Al)′, and the other poor in aluminum (Al)″.

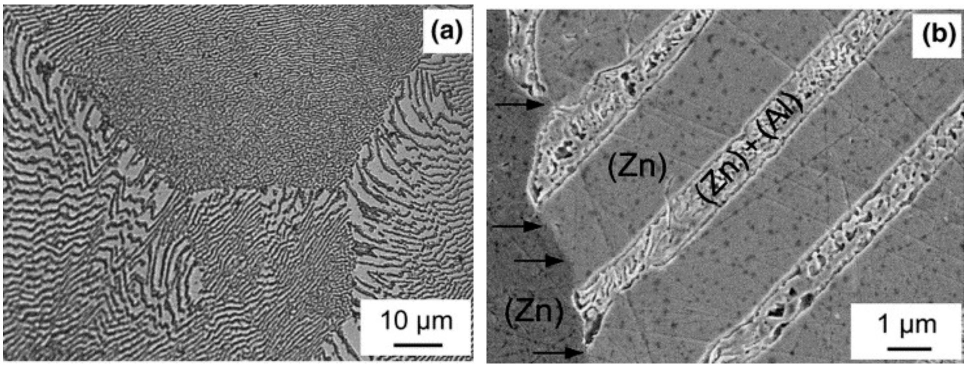

**Figure 2.** Light (**a**) and SEM (**b**) micrographs of the solidified Zn–5 wt% Al alloy. The black arrows in (**b**) show the boundary between grains of the Zn-rich phase. Reprinted with permission from Ref. [17]. Copyright 2004 Elsevier.

During annealing, the microstructure evolves toward an equilibrium state. This process is controlled by diffusion in a solid state and, therefore, takes a long time (about one month in Ref. [17]). In the case of GB wetting by the liquid phase, the equilibration includes diffusion through the melt, and an annealing time of half an hour can be long enough [12–16]. Thus, the system tends to minimize its total free energy. First, the area of (Al)″/(Zn) interphase boundaries in the eutectic colonies should decrease. During this process, the eutectic plates of the (Al)″ phase disintegrate into separate elongated particles, i.e., they are spheroidized (Figure 3 [17]). The former eutectic colonies turn into large grains of the zinc-rich phase (Zn) (it looks bright in the micrograph). The aluminum-based solid solution (Al) appears dark in the micrograph. It, in turn, undergoes a monotectoid transformation (Al) → (Al)′ + (Al)″ upon cooling after annealing.

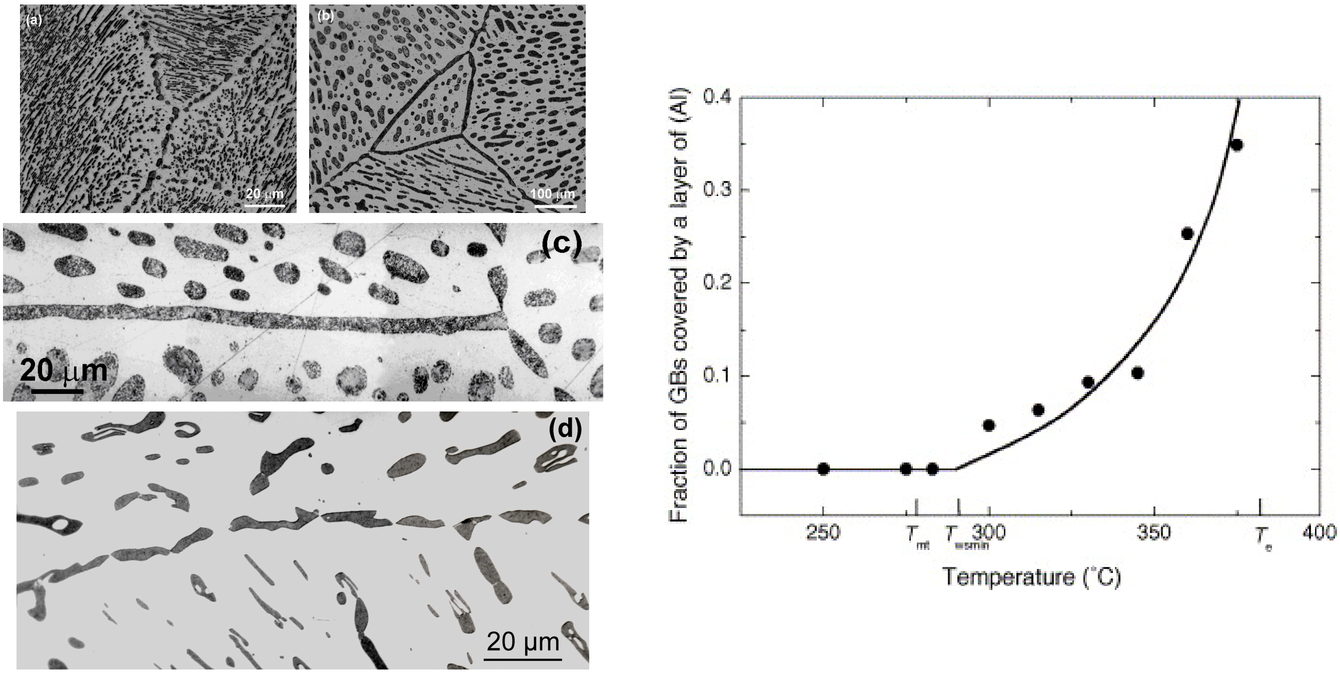

(**e**)

**Figure 3.** Light micrographs of the Zn–5 wt% Al alloy annealed at (**a**) 250, (**b**) 375, (**c**) 345, and (**d**) 283 °C. (**e**) The dependence of the fraction of (Zn)/(Zn) GBs completely wetted by the layer of the (Al) phase on temperature. Reprinted with permission from Ref. [17]. Copyright 2004 Elsevier.

Second, the boundaries between eutectic colonies should also equilibrate. It turns out that these boundaries between eutectic colonies are now the boundaries between large (Zn) grains. They are of two types. In the first case, they contain a chain of dark particles of the second solid phase, rich in other solid phases and aluminum. At other boundaries between zinc grains, a continuous interlayer of a second solid phase rich in aluminum (Al) is observed (Figure 3c). This is a case of complete wetting of the Zn/Zn GB phase by a second solid phase rich in aluminum.

Thus, we can clearly emphasize the role of wetting (it concerns thermodynamic equilibrium and determines the driving force for diffusion). Diffusion, in turn, determines the rate of equilibration (slow in the wetting by the solid phase and quick in the wetting by the melt).

At this point, the difference between a free thin plate of an aluminum-rich phase and a plate of the same phase at the grain boundaries should be emphasized. Thus, thin plates of an aluminum-rich phase formed as a result of eutectic crystallization are unstable during prolonged annealing and break up into separate pieces, which, upon further annealing, become spheroidized and approach a ball shape. This is especially well seen in Figure 3c above and below the GB, running horizontally in the middle of the micrograph. On the contrary, in the case of complete GB wetting, new thin plates of the aluminum-rich phase are formed at the grain boundaries. In several binary titanium alloys, the thickness of such grain boundary plates has been measured. It increases with annealing as the square root of the annealing time [96,98]. This means that the thickening of such plates is controlled by volume diffusion.

As the annealing temperature rises from the monotectoid decomposition temperature of 277 °C to the eutectic transformation temperature of 381 °C, the fraction of zinc GBs that are completely wetted by the aluminum-rich phase (Figure 3e) also grows. However, it does not reach 100% since the temperature interval of the specified two-phase zone on the aluminum-zinc phase diagram is small.

It is interesting to note how the energy of an individual boundary in zinc affects the wetting parameters. The micrograph in Figure 4a shows a curved (Zn)/(Zn) GB. It is known that the GB strongly depends on its inclination, especially in such anisotropic materials as zinc. Indeed, we see in Figure 4a as the GB of one inclination (marked with letters C–B) contains a chain of particles of the (Al) phase, while a GB with another inclination (marked with letters B–A) contains a continuous interlayer of the (Al) phase. This means that the GB energy $\sigma_{GB}$ is lower in the first section and higher in the second. As a result, in the second section, the GB energy $\sigma_{GB}$ turns out to be higher than the energy of two interphase boundaries $2\sigma_{(Al)(Zn)}$, and as a result, it is replaced by an interlayer of a darker (Al) phase. The second part of the same figure (Figure 4b) shows Zn/Zn twin boundaries. They are clearly visible in microstructures since they form a set of twin plates. Twin boundaries are known to have the lowest energy among other GBs [145]. Indeed, we see that lenticular particles of the second phase are formed along these boundaries. Moreover, these lenticular particles are even slightly turned and do not lie exactly in the plane of the twin GB. Such a rotation is obviously determined by the energy anisotropy of the aluminum-zinc interphase boundary.

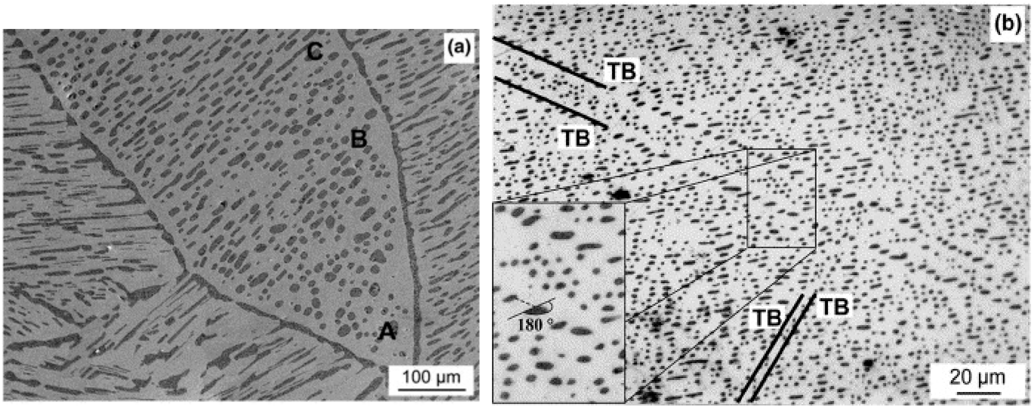

**Figure 4.** Light micrographs showing (**a**) the curved Zn/Zn GB in a sample annealed at 375 °C and (**b**) twin Zn/Zn GBs in the sample annealed at 375 °C. Reprinted with permission from Ref. [17]. Copyright 2004 Elsevier.

It has been observed in aluminum-zinc, aluminum-magnesium, and magnesium-rare-earth metals systems, as well as in some titanium alloys (Ti–Cu, Ti–Fe) and steels. Refs. [17,21,37,94,98,127] that the fraction of GBs completely wetted by other solid phases increases with increasing temperature. Thus, Figure 5 shows the SEM micrographs of Ti-Fe alloys annealed at 695 °C [98]. The α-Ti phase appears dark, and the β-Ti phase appears bright in these micrographs. Some β/β GBs are completely wetted by the second solid phase α-Ti. Letter C marks some of theses completely wetted GBs. Other β/β GBs are partially wetted by the α-Ti phase (marked by letter P). Such GBs contain the chain of lenticular α-Ti precipitates. The fraction of completely wetted β/β GBs in different Ti−Fe alloys increases with increasing temperature (see Figure 6).

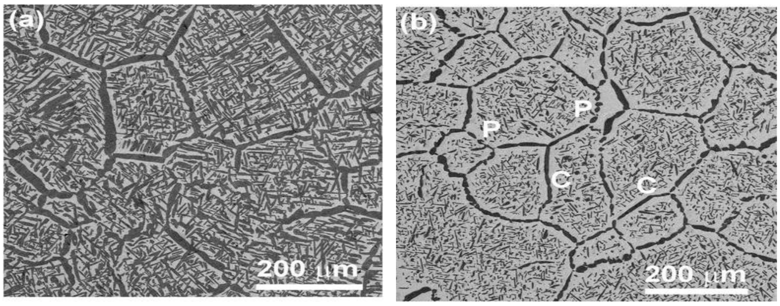

**Figure 5.** The microstructure of Ti–Fe alloys annealed at 695 °C, 1032 h. (**a**) Ti–4.5 wt% Fe alloy, (**b**) Ti–9 wt% Fe alloy. The β-Ti phase looks bright in these SEM micrographs, and the α-Ti phase is dark. Letter C shows the GBs between grains of the β-Ti phase completely covered (wetted) by continuous layers of other solid phases of α-Ti. Letter P shows GBs between grains of the β-Ti phase containing the chains of lenticular α-particles. They are partially wetted by the α phase. Reprinted with permission from Ref. [98]. Copyright 2018 Springer.

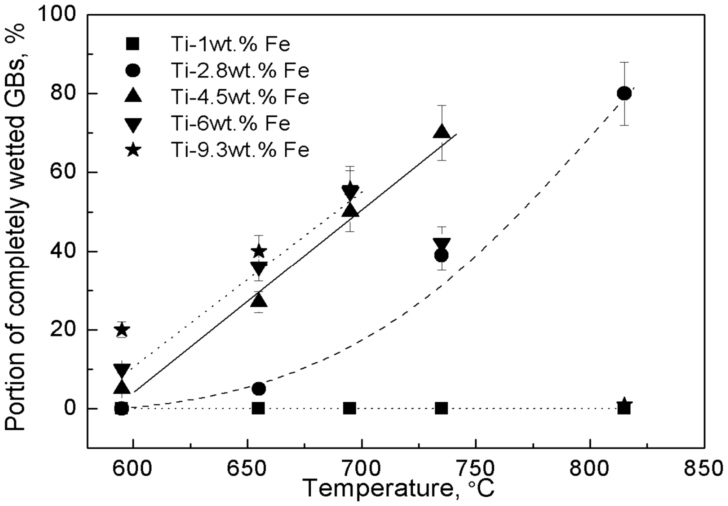

**Figure 6.** The fraction of completely wetted β/β GBs in different Ti−Fe alloys increases with increasing temperature. Reprinted with permission from Ref. [98]. Copyright 2018 Springer.

## 3. Transition from Incomplete to Complete GB Wetting with Decreasing Temperature

When GBs are wetted by the second liquid phase, the free energy of the interface between the solid and liquid phases 2$\sigma_{SL}$ always decreases with increasing temperature faster than the GB energy $\sigma_{GB}$. That is why the transition from incomplete wetting by the liquid phase to a complete one in individual GBs always occurs with increasing temperature. If the second phase is solid, then the energy of two interphase boundaries two $\sigma_{SS}$ does not always have to decrease faster with increasing temperature than the free energy of the grain boundary $\sigma_{GB}$. The free energy $\sigma_{GB}$ can decrease with increasing temperature faster than the energy two $\sigma_{SS}$ (see the diagram in Figure 1b). In this case, the transition from incomplete GB wetting to a complete one can occur without an increase but instead with a decrease in temperature. An example of such a phenomenon can be observed in the same aluminum-zinc system. Now we will consider another two-phase region, namely below the monotectoid transformation $T_{mon}$ = 277 °C, where the (Al)′ and (Zn) phases are in equilibrium (Figure 7a). In SEM micrographs of samples annealed at 260 and 190 °C, the aluminum-based phase appears dark, while the zinc-based phase appears light (Figure 7b,c). One can see that in the sample annealed at a higher temperature of 260 °C (Figure 7b), the (Al)′/(Al)′ boundaries contain lenticular zinc particles. They form the non-zero contact angle θ > 0 with (Al)′/(Al)′ GBs. It can be seen that both large (about 5 μm in size) and very small zinc particles less than a micron in size are located at these GBs. This situation corresponds to incomplete wetting of (Al)′/(Al)′ GBs by solid zinc. Figure 7c shows a sample annealed at 190 °C. In this case, the contact angle $\theta$ of the flat layers of the zinc-based phase is almost close to zero. Thus, as the temperature decreases, there is a transition from incomplete wetting of the (Al)′/(Al)′ boundaries by the second solid phase Zn to complete one.

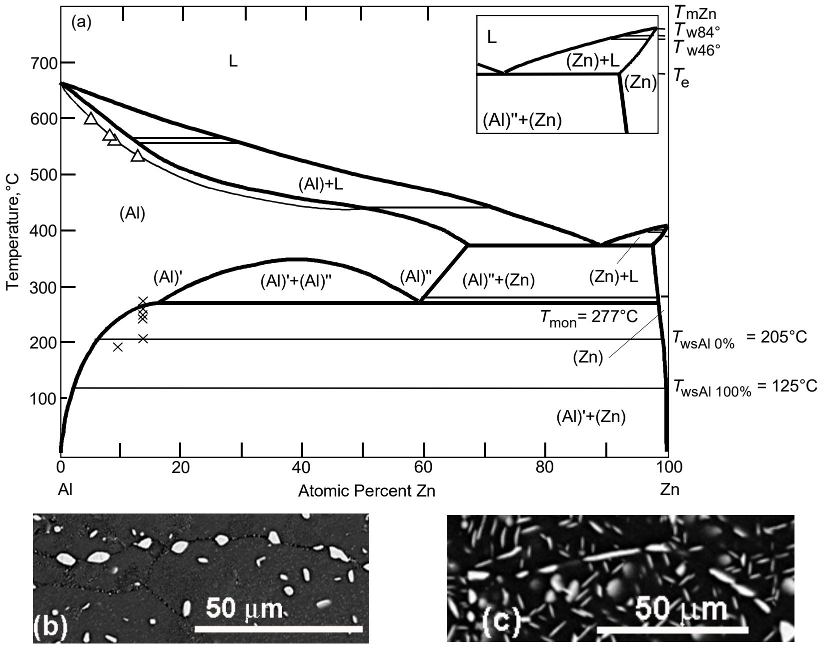

**Figure 7.** (**a**) Al–Zn phase diagram with thick lines showing the bulk phase transitions and thin lines for GB phase transformations. The inset shows the Zn-rich corner of the diagram. Triangles denote data for GB prewetting line. Crosses mark the points for the measurements of $\theta$ between Zn particles and (Al)′/(Al)′ GBs. The values of $T_{\text{wsAl0\%}}$ = 205 °C and $T_{\text{wsAl100\%}}$ = 125 °C were obtained using extrapolation of $\theta$ (see Figure 8). SEM micrographs show the morphology of GB Zn precipitates at (**b**) 260 °C and (**c**) 190 °C. Zn particles appear bright, and (Al)′ matrix appears dark. Reprinted with permission from Ref. [16]. Copyright 2011 Springer.

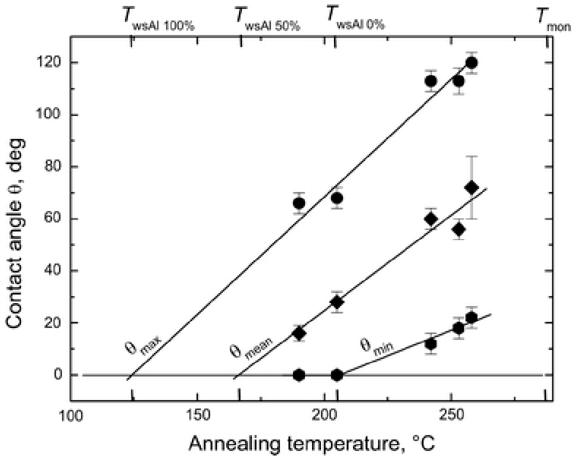

**Figure 8.** Temperature dependence on the contact angle $\theta$ between (Zn) particles and (Al)′/(Al)′ GBs. The maximal $\theta_{\text{max}}$ (circles), mean $\theta_{\text{mean}}$ (diamonds), and minimal $\theta_{\text{min}}$ (hexagons) $\theta$ values are shown. The value $\theta_{\text{min}}$ of minimum contact angle reaches zero at $T_{\text{wsAl 0\%}}$ = 205 °C. Extrapolating the maximal contact angle $\theta_{\text{max}}$ to the low temperatures gives the minimal temperature $T_{\text{wsAl100\%}}$ of the GB wetting transition. It is $T_{\text{wsAl100\%}}$ = 125 °C for the extrapolation down to $\theta$ = 0. Below this temperature of 125 °C, all GBs (Al)′/(Al)′ (Al)/(Al) would be completely wetted by solid (Zn). Reprinted with permission from Ref. [16]. Copyright 2011 Springer.

Figure 8 shows the temperature dependence of the minimum (hexagons), average (diamonds), and maximum (circles) values of the contact angle θ between zinc particles and the (Al)′/(Al)′ GBs. All these values decrease with decreasing temperature. This means that the transition from incomplete to complete GB wetting occurs with decreasing temperature. Moreover, these dependences make it possible to determine at what temperature the first Al GBs begin to appear wetted with a zinc-based phase. This can be achieved using the dependence for the minimum contact angle (hexagons). This temperature is approximately 210 °C. The dependence for the maximum contact angle θ in a polycrystal (circles) makes it possible to determine the temperature below which all (Al)′/(Al)′ GBs should be wetted by interlayers of the Zn solid phase. Unfortunately, in the Al−Zn system, this value can only be determined by extrapolation. It is about 125 °C. It must be extrapolated because the equilibration processes at such low temperatures are too slow. Already at a minimum annealing temperature of about 190 °C, its duration reached half a year. Thus, in the example of the aluminum-zinc phase diagram, we see that the fraction of GBs completely wetted by the other solid phase can either increase or decrease with increasing temperature.

## 4. Non-Monotonous Transition from Incomplete to Complete GB Wetting with Increasing Temperature

The diagram in Figure 9 shows that the temperature dependence of the free energy of the grain boundary in the α-phase $\sigma_{\alpha\alpha}(T)$ and that of the interphase boundary of two solid phases $2\sigma_{\alpha\beta}(T)$ can intersect more than once, for example, twice. In this case, there are two temperatures of their intersection $T_W$ and $T_{DW}$.

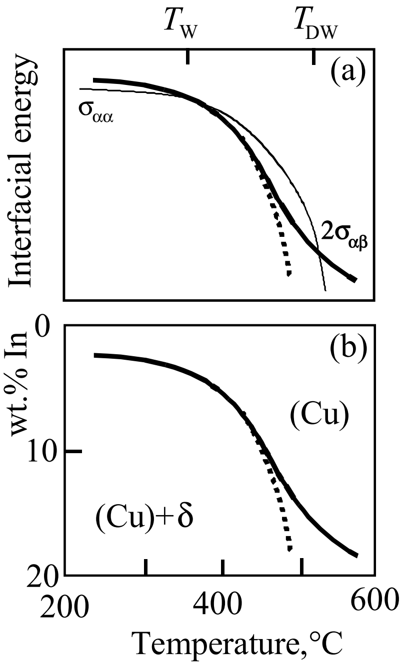

**Figure 9.** (**a**) Schematic temperature dependences for the GB energy $\sigma_{\alpha\alpha}$ (thin line) and energy $2\sigma_{\alpha\beta}$ of interphase boundaries (Cu)/δ (thick line). They intersect two times at $T_W$ = 370 °C and $T_{DW}$ = 520 °C. (**b**) The solubility limit of In in (Cu) solid solution (solid line). The dashed line shows the typical shape of the solubility limit in the phase diagrams without non-monotonous GB wetting. Reprinted with permission from Ref. [89]. Copyright 2014 Springer.

For the case shown in the diagram, this means that below the first crossing temperature $T_W$, the α/α boundary will not be completely wetted by the second solid phase β. Between the intersection temperatures $T_W$ and $T_{DW}$, the α/α GB will be completely wetted by the second solid phase β. In other words, the β phase forms a continuous layer at the boundary separating the α grains from each other. Above the second intersection temperature $T_{DW}$

of the $\sigma_{\alpha\alpha}(T)$ and $2\sigma_{\alpha\beta}(T)$ dependences, the $\alpha/\alpha$ GB will again be incompletely wetted, and the second phase $\beta$ will again form a chain of lenticular particles in the $\alpha/\alpha$ GB.

In the copper-indium system, we deal again with a structure consisting of eutectic colonies before annealing (Figure 10). After prolonged annealing, the boundaries between large copper grains become clearly visible. Copper appears dark in the micrographs. Particles of intermetallic compound $\delta$ appear bright in the micrographs. They exist in the bulk of copper grains as well as at the Cu/Cu GBs. The micrograph of the alloy annealed at 360 °C (Figure 10a) clearly shows that the boundaries between copper grains contain chains of white intermetallic particles $\delta$. This behavior witnesses the partial wetting of Cu/Cu GBs by the solid intermetallic phase $\delta$.

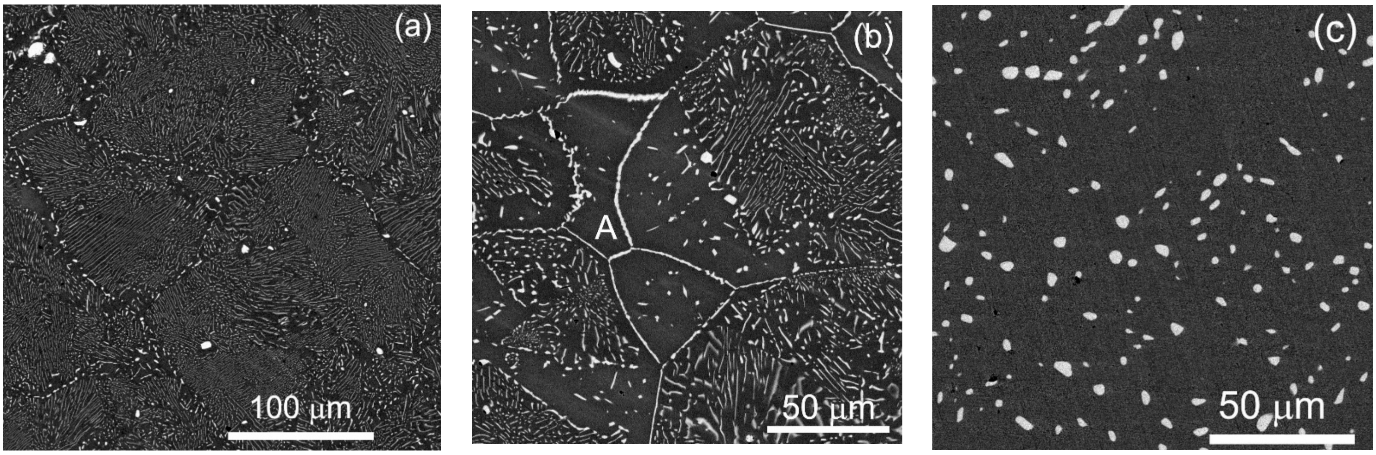

**Figure 10.** Microstructure of annealed Cu–In alloys (**a**) Cu–8 wt% In, 360 °C. (**b**) Cu–12 wt% In, 450 °C, letter A marks the completely wetted (Cu)/(Cu) GB. (**c**) Cu–17.5 wt% In alloy, 520 °C. SEM micrographs are reprinted with permission from Ref. [89]. Copyright 2014 Springer.

At temperatures above 370 °C, the non-interrupted layers of intermetallic compound $\delta$ exist in the Cu/Cu GBs (Figures 10b and 11a). This means the Cu/Cu GBs are completely wetted by the solid intermetallic compound $\delta$. The fraction of completely wetted Cu/Cu GBs grows with increasing temperature and reaches almost 100% around 450 °C (Figure 11, black squares). However, if the annealing temperature increases above 450 °C, the portion of completely wetted Cu/Cu GBs begins to decrease. Thus, above 520 °C, the completely wetted boundaries disappear again. In the micrograph of the sample annealed at 520 °C (Figure 10c), we again see only individual particles and not continuous interlayers at the boundaries. Thus, two new lines of GB phase transformations appear on the copper-indium phase diagram (Figure 11b). The first at $T_W$ = 370 °C corresponds to the beginning of complete wetting of the Cu/Cu GBs by the intermetallic compound, and the second $T_{DW}$ = 520 °C marks the upper border of the region where complete GB wetting is observed. Above 520 °C and below 370 °C, there are no copper grain boundaries in the system completely wetted with intermetallic compound $\delta$.

A non-monotonic increase in the fraction of grain boundaries completely wetted by the second solid phase with increasing temperature is also observed in some titanium alloys (Ti–Co, Ti–Cr) [92,98], Co–Cu alloys [77], as well as in the low-alloy steel [37]. Cementite wetting of GBs in steels is an important topic that has been reported by various authors, particularly in hyper eutectic steels and stainless steels [46,49] (see also the discussion in Section 6).

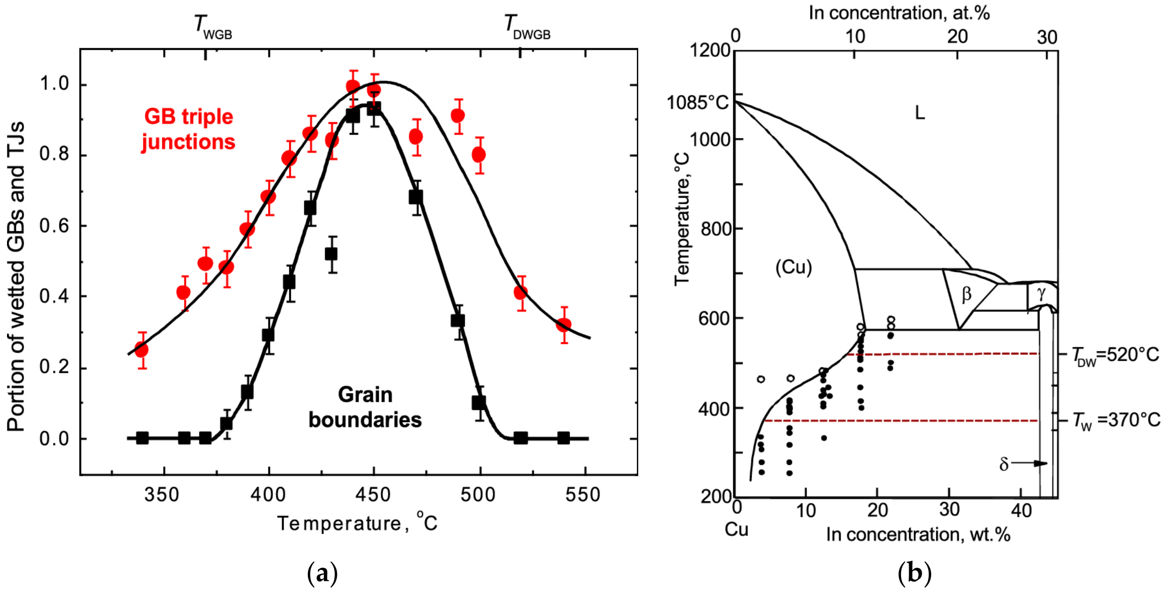

(**a**) (**b**)

**Figure 11.** (**a**) Temperature dependences of (**a**) the fraction of (Cu)/(Cu) GBs (black squares) and GB triple junctions (TJs) (red circles) completely wetted by the layers of solid intermetallic δ-phase. (**b**) Cu–In phase diagram. Circles indicate the annealings of various alloys in the two-phase (filled symbols) and one-phase (open symbols) areas. Reprinted with permission from Refs. [87,89]. Copyright 2021 and 2014 Springer.

## 5. Wetting of Grain Boundary Triple Junctions by the Second Solid Phase

The grain boundaries form so-called triple junctions (TJs). A triple GB junction is a linear defect along which three adjacent grains meet. At triple junctions, complete and incomplete wetting by a liquid or second solid phase can also be observed. Figure 12 shows various combinations for complete and incomplete wetting of three-grain boundaries and their common triple junction. In the case of complete TJ wetting, a triangular prism of the second phase substitutes the triple junction. With incomplete wetting, a chain of triangular particles of the second phase is visible along the triple junction.

In the case of complete GB wetting, an interlayer of the second phase is formed along the GB, and the condition for complete GB wetting is that the GB energy is higher than the energy of two interphase boundaries $\sigma_{GB} > 2\sigma_{SS}$ (Figure 13a,b). When the triple junction is completely wetted, a triangular prism of the second phase is formed on it (Figure 13d). It replaces the star of three GBs that was previously inside it (Figure 13c). Thus, the wetting conditions for a triple junction are as follows: $\sigma_{GB} > \sqrt{3}\ \sigma_{SS}$. In other words, the free energy of the wetted GB should not be higher than $2\sigma_{SS}$, but it should be higher than $\sqrt{3}\sigma_{SS}$. The TJ wetting condition $\sigma_{GB} > \sqrt{3}\ \sigma_{SS}$ is not as stringent as the GB wetting condition $\sigma_{GB} > 2\sigma_{SS}$ because the root of three is less than two. Therefore, in the scheme of temperature dependences of free energy of interphase boundaries and GBs (Figure 13f), the condition for complete wetting for TJs is located below the line for complete GB wetting. This means that the transition temperature from incomplete to complete TJ wetting should be lower than the transition temperature from incomplete to complete GB wetting.

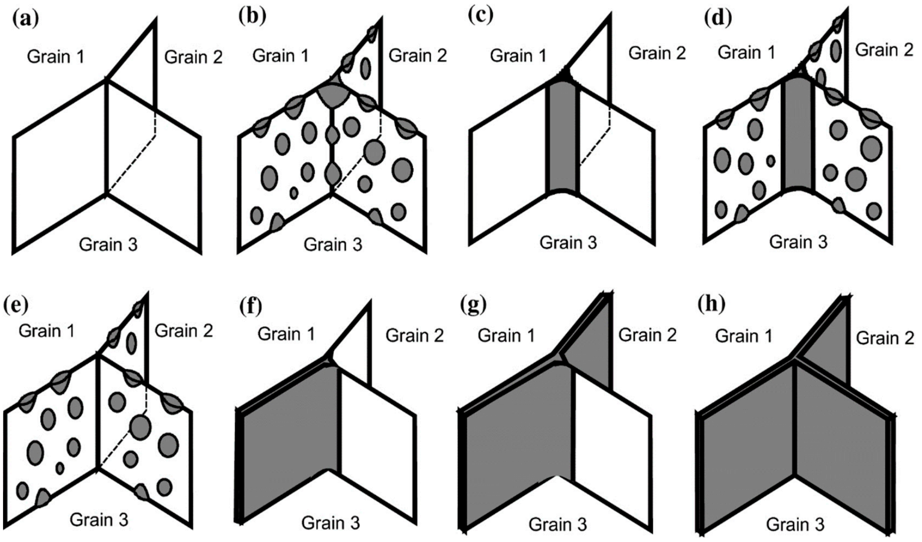

**Figure 12.** GB triple junction among grains 1, 2, and 3. Grey color marks the liquid phase. (**a**) Dry TJ contacting three dry GBs. (**b**) Incompletely wetted GB TJ in contact with three incompletely wetted GBs. (**c**) Completely wetted GB TJ contacting dry GBs. (**d**) Completely wetted TJ contacting three incompletely wetted GBs. (**e**) A dry GB TJ contacting three incompletely wetted GBs. (**f**) Fully wetted GB TJ contacting one fully wetted GB. (**g**) Fully wetted GB TJ contacting two fully wetted GBs. (**h**) Fully wetted GB TJ contacting three fully wetted GBs. Reprinted with permission from Ref. [87]. Copyright 2021 Springer.

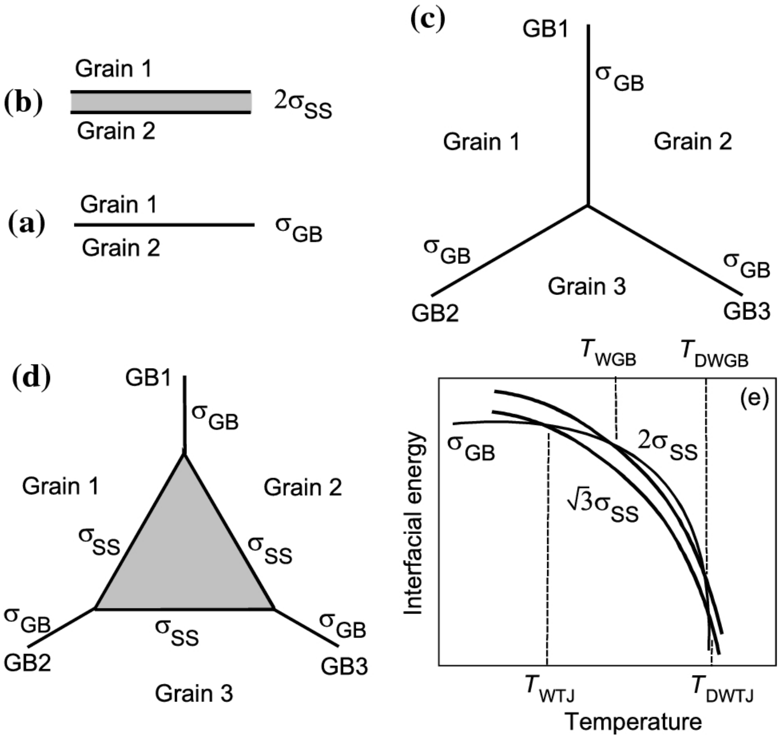

**Figure 13.** (**a**) Non-wetted GB having energy $\sigma_{GB}$. (**b**) Fully wetted GB (it is substituted by a layer of other solid phase and two interphase boundaries having energy $2\sigma_{SS}$). (**c**) Non-wetted GB TJ, which is constructed of three GBs of the same energy $\sigma_{GB}$. (**d**) GB TJ substituted by the triangular prism of solid phase (it is the case of complete wetting of GB TJ). (**e**) Temperature dependence for $\sigma_{GB}$, $2\sigma_{SS,}$ and $\sqrt{3}\sigma_{SS}$ (being the energy of interphase boundaries of two solid phases in the triangular prism). Such a triangular prism substitutes the GB TJ in case of its complete wetting. Reprinted with permission from Ref. [87]. Copyright 2021 Springer.

Such a phenomenon for the wetting of GB TJs by a melt was observed experimentally for the first time for aluminum-based alloys [87]. Indeed, it turned out that the difference in temperature between the wetting transition for TJs and GBs is quite measurable and reaches about 15–20 °C. The wetting of GB TJs by the other solid phase was first studied on magnesium alloy EZ33A [125]. Figure 14a shows the microstructure of such an alloy. In the micrograph, the magnesium matrix appears dark, while the particles of the second phase, containing different metals, appear light. Letters in Figure 14a denote differently wetted triple junctions. These letters correspond to the wetting schemes for the GBs and TSs in Figure 12. As a result of the experiments carried out at temperatures from 150 to 400 °C, it turns out that the fraction of completely wetted boundaries between magnesium grains is everywhere lower than the fraction of completely GB TJs (Figure 14b). Above, we considered the copper-indium system, where the transition from incomplete to complete GB wetting by solid intermetallic compound δ occurs non-monotonically. For example, the (Cu)/(Cu) GBs completely wetted with intermetallic compound δ exist in the temperature range between 370 °C and 520 °C (Figure 11). However, above 520 °C, the completely wetted (Cu)/(Cu) GBs disappear again. In the diagram shown in Figure 13, a case is considered of how the energy curves of interfacial boundaries, grain boundaries, and triple junctions may look. This scheme predicts that the temperature range in which there will be GB TJs completely wetted by other solid phases may be wider than the temperature range in which there are completely wetted GBs.

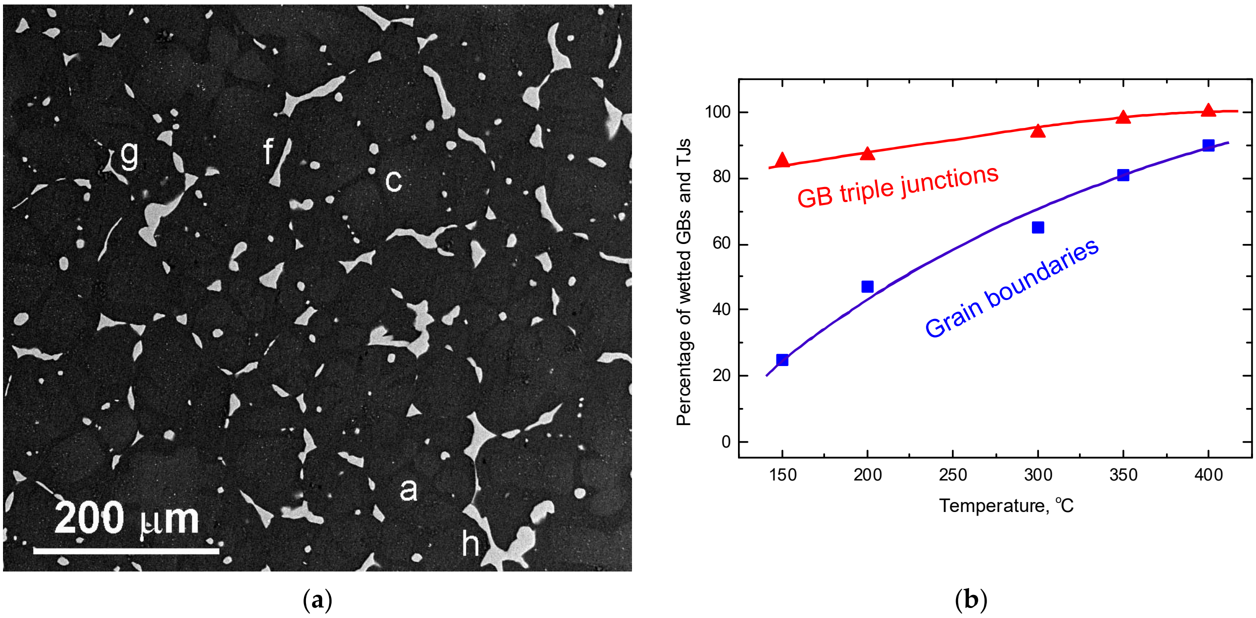

(**a**) (**b**)

**Figure 14.** (**a**) Microstructure of the EZ33A alloy annealed at 150 °C (SEM micrograph). The mg-rich matrix appears black; the GBs and TJ wetting layers appear bright. The letters a, c, f, g, h mark differently wetted GBs and TJs according to the scheme in Figure 12. (**b**) Fraction of wetted GBs (filled squares, lower curve) and GB TJs (filled triangles, upper curve) at different temperatures. Reprinted with permission from Ref. [125]. Copyright 2020 Springer.

Indeed, it was observed experimentally that the first completely wetted GB TJs appear in this system below 300 °C [87]. At the same time, the first fully wetted GBs appear only at 375 °C. The fully wetted GBs disappear at about 520 °C. At this temperature, there are still many fully wetted triple junctions in the system (Figure 15). Figure 11 clearly shows that the portion of completely wetted TJs at all studied temperatures is higher than the portion of completely wetted GBs. Moreover, the curve for temperature dependence is much broader for triple junctions than for GBs. The curve for TJs seems to cover from above and from both sides of the curve for completely wetted grain boundaries.

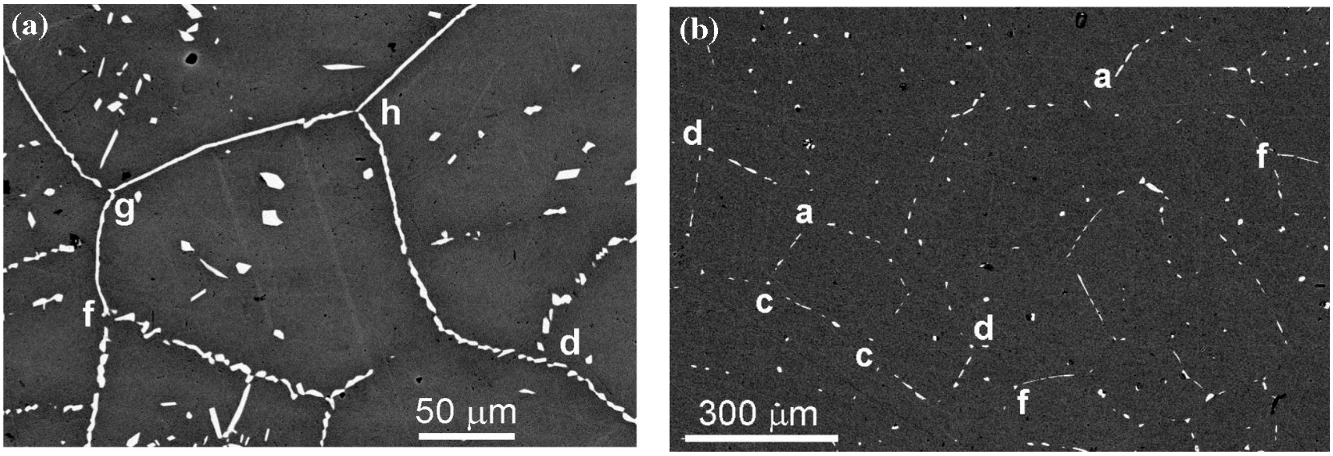

**Figure 15.** Microstructure of Cu–In alloys annealed at 430 °C (**a**) and 520 °C (**b**). The (Cu) matrix appears black in SEM micrographs. The *δ*-phase wetting the GBs and TJs appears white. The letters a, c, f, g, h mark differently wetted GBs and TJs according to the scheme in Figure 12. Reprinted with permission from Ref. [87]. Copyright 2021 Springer.

## 6. Influence of GB Wetting by the Second Solid Phase on the Properties of Materials

GB wetting by the second solid phase can have a strong influence on the properties of materials, including Al alloys [18,20,22,23,25–35], Fe-based alloys and steels [36,38–76], Co- and Ni-based alloys [78–85], Cu alloys [86,88,90], Ti- and Zr-based alloys [91,93,95,97,99–123], Mg alloys [124,126,128–131], as well multicomponent and high-entropy alloys [132,134,136–144].

For example, it was observed by Qin et al. that the shape of the second phase(s) in the precipitation-hardenable Al–0.31Mg–0.68Si wt% alloy strongly depends on the cooling rate [18]. The changing cooling rate drives the GB wetting transition and, thus, modifies the hardening of the studied Al–Mg–Si alloy. Gao et al. observed that the precipitates in the Al–Cu–Li-based alloys significantly influence the behaviors in the subsequent processing and heat treatment procedures and, therefore, potentially expand their applicability for the aerospace industries owing to their relatively low density and excellent performances [22]. The studied alloy contained Cu–2.66, Li–1.31, Mn–0.27, Zr–0.11, Mg–0.09, Ti–0.03, and Fe–0.04 wt%. The air-cooled sample was dominated by T-phase ($Al_{20}Cu_2Mn_3$), and $\beta'$-phase ($Al_3Zr$) precipitated at high temperature, accompanied by naturally aged $\delta'$-phase ($Al_3Li$). In the sample cooled with the furnace, in addition to the T and $\delta'/\beta'$ phases, predominant are the precipitates of micrometer-scale $T_1$-phase ($Al_2CuLi$) and some of $\theta'$-like ($Al_2Cu$) phase. The shape of GB precipitates of all these phases differed, changing between complete and partial GB wetting [22].

GB wetting by the second solid phase was also observed in an ER4043 Al-based alloy after wire and arc additive manufacturing [20], Al–Cu–Li alloy after slowed cooling from 520 °C [25], during GB precipitation of $T_1$-phase during quenching in a 2A97 aluminum alloy (Figure 16a) [26], after non-isothermal aging of Al–4.44 wt%Zn–1.57 wt% Mg–0.37 wt%Mn–0.24 wt%Cr–0.12 wt%Cu–0.10 wt%Zr–0.05 wt%Si–0.09 wt%Fe alloy (Figure 16b) [28], in an Al–Cu–Mg alloy after friction stir spot processing [30], in an Alnico alloy compounded by hot isostatic pressing and hot rolling followed by the traditional heat treatment [31], in a high-strength AA7075–H18 alloy [32], in Al–1.5B–3.7Ti–1Mn and Al–2Mn–1Fe alloys [33], in an Al–2.5Mn–3.3Cu–0.5Zr (wt%) produced with the aid of electromagnetic casting [34], and during superplasticity of an Al–15 Zn (at%) alloy [35].

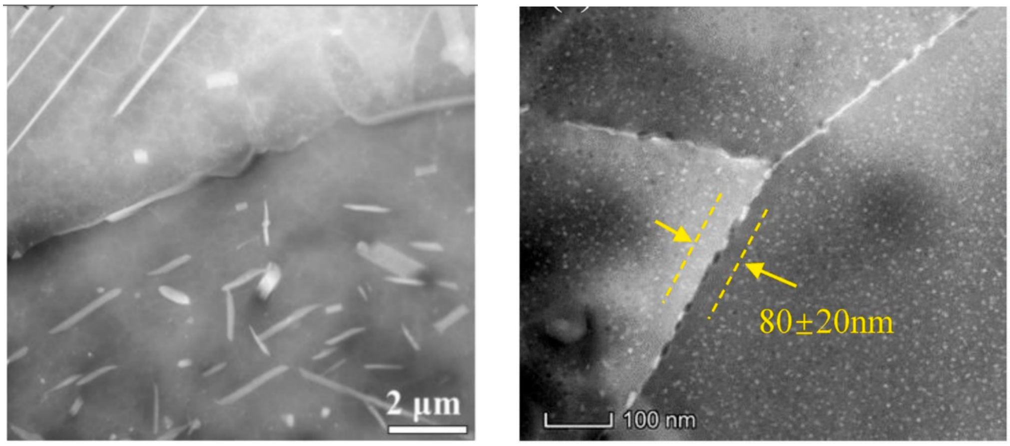

(**a**) (**b**)

**Figure 16.** (**a**) GB precipitation of $T_1$-phase during quenching in a 2A97 aluminum alloy. Reprinted with permission from Ref. [26]. Copyright 2021 Elsevier. (**b**) HAADF-STEM images of intergranular precipitates after non-isothermal aging of an Al–Mg–Zn alloy. Yellow lines and arrows show the precipitate-free zone [28]. Reprinted with permission from Ref. [28]. Copyright 2021 Elsevier.

The hardness of boronized AISI 1045 steel depends on the shape of iron borides in a GB Fe-based matrix [36]. GB carbides (such as Mo-rich $M_6C$ and Cr-rich $M_{23}C_6$ phases) in the metal after multi-pass welding can initiate a stress rupture in the 9%Cr–CrMoV welded joints [40]. $M_{23}$C6, MX carbides, σ phases, Z phase, and ε-Cu phase precipitate in the Super 304H austenitic stainless steel after long-term aging. The precipitation (including different GB precipitates) changes the creep strength [58]. GB wetting by other solid phases was also observed in TiC-reinforced steel matrix composite [38], 316L stainless steel [39], Fe–2Cu–1.5Ni–1.5Mn low-alloyed steel [41], boron-alloyed 304 and 316 stainless steels [42], Fe–0.2%C–0.92%Cr–0.52%Mn–0.24%Si–0.16%Mo alloy [43], χ-phase between ferrite grains in super duplex stainless steel S32750 [44], gas nitrided die steel modified by a plasma detonation [45], hydrogen treated 304 austenitic stainless steel [47], the experimental Fe–2.03Mn–1.92Cu–1.35Ni–1.04Al–0.84Si–0.26–0.16NbMo–0.16C alloy annealed at 700 and 720 °C [48].

In Ref. [46], the high-carbon steel with 0.77 wt%C, 0.59 wt%Mn, 0.36 wt%Cr, and 0.21 wt%V has been investigated. It has been confirmed that vanadium addition results in the formation of GB ferrite films, even in the eutectoid composition range. It has been argued that this ferrite is the product of eutectoid transformation and is not a pro-eutectoid ferrite. The structure observed by Han et al. [46] was formed by continuous cooling during eutectoid decomposition. Therefore, the ferrite GB layers could indicate the wetting of austenite GBs before the eutectoid decomposition rather than the ferrite wetting of cementite GBs afterward. In hypereutectoid steel (with 1.24 wt%C, 0.25 wt%Si, 0.26 wt%Mn, 0.17 wt%Cr, 0.028 wt%Mo, 0.12 wt%Ni, 0.025 wt%Al, 0.19 wt%Cu, 0.019 wt%P, 0.015 wt%S) annealed at 1100 °C. After cooling through the austenite+cementite area of the phase diagram, continuous GB layers of cementite formed in the austenite GBs [49]. It is an important indication of the wetting of austenite/austenite GBs by cementite. The ferrite completely wets the grain boundaries of austenite transformed into perlite in the medium-carbon micro-alloyed steel (Fe–0.47 C–0.92 Mn–0.32 Si–0.21 Cr–0.006 P–0.046 S–0.09 V–0.022 Ti–0.015 N) after heating to 1000–1300 °C with different rates of 0.1–1.0 K/s. With an increasing heating rate, the GB ferrite layers become thinner (Figure 17) [50].

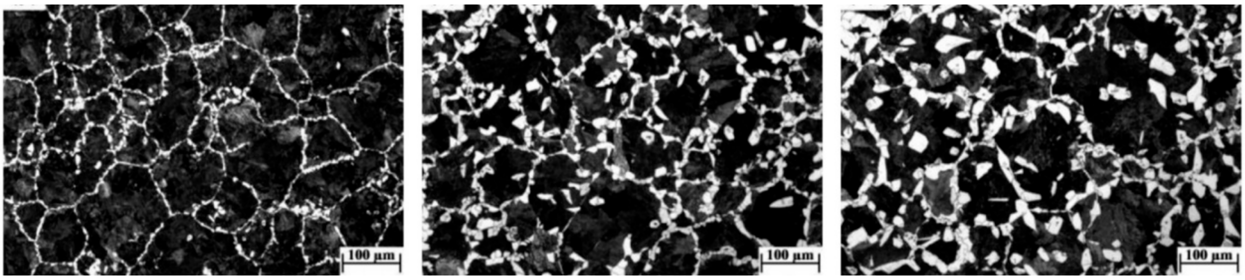

**Figure 17.** Ferrite network between grains of austenite transformed into perlite after heating to 1300 with a heating rate of 1.0 K/s (**left**), 0.3 K/s (**middle**), and 0.1 K/s (**right**). Reprinted with permission from Ref. [50]. Copyright 2021 Elsevier.

The continuous and discontinuous GB layers of a second phase were observed also in the Fe–6.63Mn–0.077Si–0.40Mo–0.021C (wt%) medium Mn steel [51], the 45 steel irradiated by electron beam [52], medium Mn steel Fe–8.9Mn–1.54Si–1Al–0.05C (wt%) [54], in 316 L stainless steel fabricated by laser powder bed fusion [55], low carbon steel with additions of TiC–$TiB_2$ nanoparticles [59], 0.02Ni and 0.44 Ni steels [60], the die steel alloyed with Si–V–Cr–Mn–Ni–Mo–Nb–Ti [61], in the iron–carbon–chromium hard coatings [62], in the coarse-grained heat affected zone of welded ultra-high strength steel [63]. The doping with alloying elements can also affect the wetting of grain boundaries. K. Han et al. studied a series of high-purity steels with varying carbon, silicon, and vanadium content [56]. The samples were austenitized for 10 min at 1050 °C and subsequently transformed at 600 °C for 3 min. The continuous and discontinuous cementite layers in GBs of austenite (transformed into perlite by cooling) are easily visible in vanadium steel (0.79C–0.22Si–0.62Mn–0.2V) and high-vanadium silicon steel (0.91Si–0.82C–0.66Mn–0.2V). On the contrary, the samples of plain carbon steel (0.72Mn–0.76C–0.23Si), silicon steel (0.96Si–0.81C–0.72Mn) as well as of, low-vanadium-silicon steel (1.01Si–0.84C–0.1V–0.73Mn) do not possess such GB cementite layers [56]. J. Yuan et al. studied the morphological evolution of carbonitrides and the effect of these precipitates on GB pinning during pseudo-carburizing an Nb–Ti–Al micro-alloyed steel [57]. Various complex carbide and nitride precipitates formed in samples austenitized at different temperatures and times. The concentration of Nb, Ti, and Al strongly influences the morphology of these precipitates, which partially wet the austenite GBs [57].

The morphology of the GB phases influences the strength as well as ductile-brittle transition temperature of ultra-high strength steel Fe–0.1 wt%C–0.015 wt%Ti–1.0 wt%Mn–0.2 wt%Si–3.0 wt% (Cr + Ni + Cu + Mo + Nb) [64]. The GB segregation and GB wetting influence the microstructure and mechanical properties (strength and ductility) of an inter-critically annealed quenching and partitioning steel [65]. The 10Cr–3Co–3W–1Mo nitrogen free creep resistant steels without B and with 90 ppm and 120 ppm of B were annealed at a temperature of 650 °C [66]. They contained GB films of Laves phase. These films did not show a detrimental effect on the material plasticity in the quasistatic tensile tests at 650 °C [66]. The transformation-induced plasticity (TRIP) steel with the composition of Fe–0.295C–0.9Si–2Mn–0.65Al–0.082V (wt%) was obtained through casting, hot forging, hot rolling, cold rolling, and two-stage annealing at 800 °C (inter-critical annealing (IA)) + 430 °C for isothermal bainitic transformation (IBT) [67]. The retained austenite (RA) in the bulk phase and GBs have the highest stability at different IBT times of 4 min. A good combination of ductility and strength is obtained in this sample [67]. The high strength low alloy steel Fe–0.16C–1.45Mn–0.20Si–2.80–0.12 (Nb + V + Ti) (Cr + Ni + Cu + Mo + Co)–0.0005B (wt%) possesses the highest density of high angle GBs at the nose temperature of bainite transformation curve. It corresponds to the cooling rate of 5 °C/s. The GB wetting phenomena were observed in the bainite+martensite mixture [67]. GB wetting by the second solid phase was also observed in $Fe_{75}Cu_{7.5}Ga_{18.5}$ alloy [69], Nb–V micro-alloyed steel [70], as-cast S31254 super austenitic stainless steels modified with boron [71], column-faced 45 steel [72], ultra-heavy E500 offshore engineering steel [73], Fe–1.3 wt% Cr–0.13 wt% C–0.56 wt% Mo alloy [74], 316 L stainless steel fabricated using the hybrid in-situ rolled wire-arc additive manufacturing (HRAM) [75] and bainitic steel with C0.31, Mn2.11, Si1.18, Cr1.19, Al0.78, Ni0.25, Mo0.26, S0.0016, P0.006 (wt%) [76].

Thulasiram et al. [80] studied the grain size refinement, texture, and tensile properties of a novel Inconel 718 alloy annealed between 500 and 800 °C. The decreased grain size and GB layers of a second solid led to the decreased cleavage size. The decreased cleavage size, in turn, increased ductility [80]. The high-temperature oxidation behavior induced by precipitation in a Ni–Y–Al alloy is also controlled by the wetting of interfaces [82]. The perfect orientation relationship between hcp $Ni_5Y$ and fcc $\gamma$-Ni phases in this Ni–Y–Al alloy resulted in the internal oxidation of Al and Y within the $Ni_5Y$-based phase. In turn, this resulted in the formation of parallel $Al_2O_3$ and $Y_4Al_2O_9$ (YAM) strips along the YAM/$Ni_5Y$ interphase boundaries in a wetting manner. It follows from these examples that the phenomenon of GB wetting by the second solid phase gives in the hands of materials engineers a new instrument to tailor the properties of a broad spectrum of two and multiphase materials. The GB wetting phenomena were observed in the CoCrFeNiMo alloys and Inconel 718 with Ni interlayer after vacuum diffusion bonding [78], in the Ni-based superalloy Inconel 718 (IN718) after delta-processing treatment (DP718) and subsequent high-temperature deformation [79], in a Ni–Y–Al alloy after high-temperature oxidation [82], in the $(Ti_{45}Ni_{55})_{100-x}Fe_x$ ($x$ = 0.5, 1, 3, 5 at%) alloy containing $X$-phase precipitates and having high hardness and high compressive strength [85], the Invar/Cu bimetal composites [88], NiTi superelastic alloy manufactured by selective laser melting [115], Cu based $Ti_2AlC$ composite [91] as well as in Bi-containing brass (Cu–3wt%Bi–30wt%Zn) [90]. The transition between discontinuous and continuous precipitation of the Cr-rich phase was observed by the annealing of solution-treated binary Ni–Cr alloys with 30%, 35%, 40%, 45%, and 50% Cr, and ternary ones doped by 0.5% third elements (Cu, Zr, Nb, Fe, and B) [81]. In some samples, this Cr-rich phase formed continuous wetting layers along matrix GBs (Figure 18).

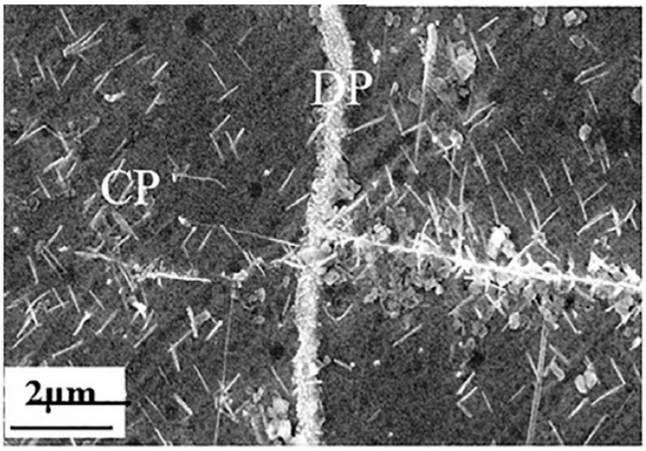

**Figure 18.** SEM micrograph of the Ni-45 wt%Cr alloy annealed at 850 °C. The Cr-rich phase appears bright and formed by discontinuous (DP) and continuous (CP) precipitation. Reprinted with permission from Ref. [81]. Copyright 2021 Elsevier.

Different heat treatment routes were studied by Zhang et al. for the Ti–6Al–4V alloy produced by additive manufacturing [101]. Its dynamic compressive strength was increased by the heat treatment process. The heat treatment also changed the dynamic compressive strength. It was isotropic before heat treatment and became anisotropic afterward. The heat treatment also reduced the strain rate sensitivity of the material by heat treatment. It correlates with mutual GB wetting of α and β phases [101]. In the (TiC + TiB+$(TiZr)_5Si_3$)/TA15 composite, after oxidation, the β-Ti phase forms the layers wetting the α/α GBs (Figure 19) [99]. GB wetting by the second solid phase was observed in a β-solidifying γ-TiAl alloy during β-α transformation [93], α-β phase transformation in a metastable TiZr based alloy [95], single-pass laser welding of 304 stainless steel and

TC4 Ti alloy with V interlayer and Cu/V bilayer [97], in the $TiAl_2$ and TiAl aluminum-rich intermetallics [100], Ti6Al4V/TiC composite coatings [102], in titanium aluminide materials manufactured by combustion and high-temperature shear deformation [103], in Ti–30.46 wt%Zr–0.73 wt%Hf–5.29 wt%Al–3.04 wt%V $\alpha + \beta$ alloy [104], in $\alpha + \beta$ Ti–4V–6Al titanium alloy [105], in Ti–80 at% W alloys [106], in 4J36/Ni/Cu/V/TC4 diffusion-bonded joints [107], the welded CP–Ti/304 stainless steel and CP–Ti/T2 bimetallic sheets [108], in the near-β Ti–5Mo–5Al–5V–1Fe–1Cr (Ti-55511) alloy [109], the hot isostatic pressed TA15 titanium alloy after solution and aging treatment [110].

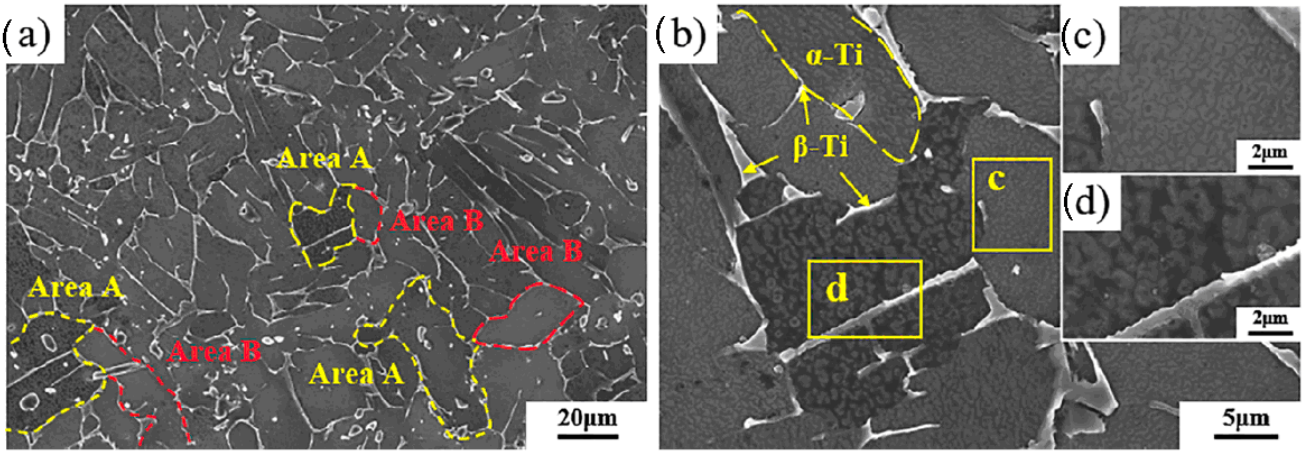

**Figure 19.** (**a**) SEM image of the oxidized (TiC + TiB + $(TiZr)_5Si_3$)/TA15 composite; (**b**) magnified view of area A and B; (**c**,**d**) magnified images of the areas c and d in (**b**). Reprinted with permission from Ref. [99]. Copyright 2021 Elsevier.

By changing the Mo content in the Ti–44Al–(0–7)Mo (at%) alloys, the different variants of mutual complete and incomplete GB wetting by the α2, γ, and $\beta_o$ phases were observed (see Figure 20) [111]. The Ti–Nb–Mo alloys with different Nb concentrations were manufactured by powder metallurgy [112]. The temperature and duration of sintering influenced the mechanical properties and microstructure of these alloys, including the morphology of GB layers of the Nb-rich phase. In Ref. [112], the microstructure and mechanical properties of a Ti–15Zr alloy (wt%) manufactured by powder metallurgy and hot extrusion were investigated. The alloy is comprised of an α-phase matrix with Zr-rich stripes distributed both in the bulk phase and between grains (GB wetting layers). The alloy had an excellent combination of ductility and strength due to the presence of Zr-rich stripes. It is because the Zr-rich stripes can hinder dislocation movements. They also strengthen the GBs. However, they cannot completely stop their movement. It is because the slip transmission could also occur across Zr-rich GB layers [112]. In Ref. [114], the TC4/Nb/Cu/316L diffusion welded joints (they were also subjected to cryogenic treatment after welding) were studied. The GB wetting in the α+β mixture in TC4 alloy is easily visible. The strength of TC4/Nb/Cu/316L joints increased as a result of cryogenic treatment [114]. The adiabatic shear bands and crack propagation mechanism have been studied in Ref. [117] in a Ti–6Al–4V alloy during hot deformation. The crack propagation is controlled by the voids and micro-cracks on prior-$\alpha/\beta_{trans}$ interphase boundaries and, therefore, by GB wetting. GB wetting by the second solid phase was observed in the Ti–Nb–Al alloys produced by spark plasma sintering and mechanical alloying with varied Ta additions [116], Ti–6Al–4V–$x$Ce ($x$ = 0, 0.1, 0.3, 0.5, 0.7 wt%) alloys [118], Ti–Ni shape memory alloys doped with boron [119], hot-deformed Ti–47Al–1.5Re–X (Cr, Mn, V, Nb) alloy [120], TC11 duplex titanium alloy (with nominal composition Ti–3.5Mo–6.5Al–1.5Zr–0.3Si) manufactured by the laser-directed energy deposition and annealed afterward at 1020 °C [121].

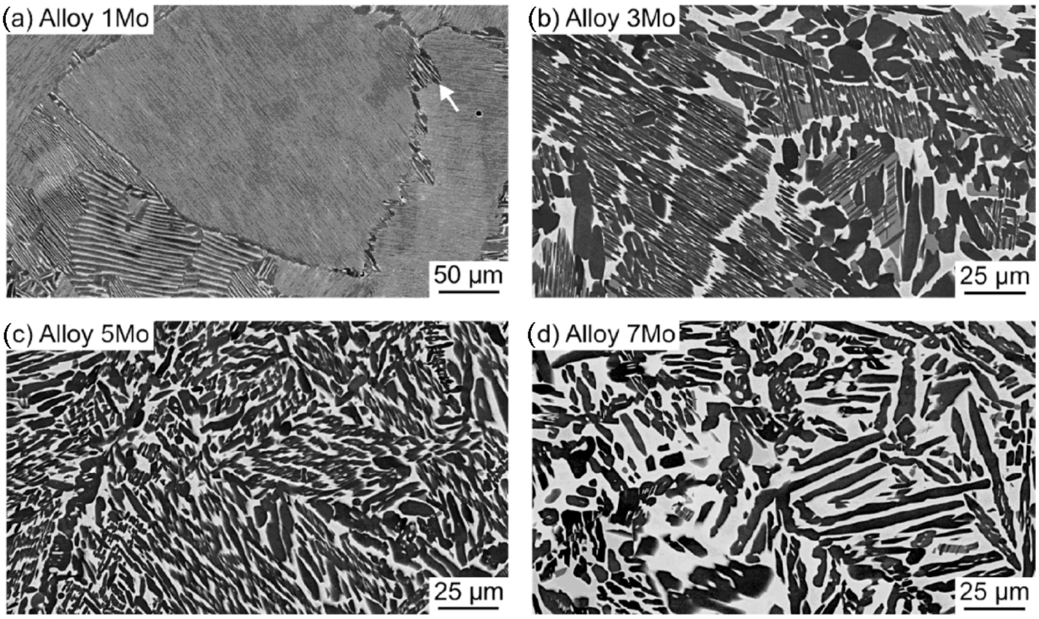

**Figure 20.** Microstructure of Ti–44Al–(0–7)Mo (at%) alloys HIP heat-treated at 1200 °C for 4 h. SEM-BSE micrographs shows that in the alloy 1Mo (**a**) only the $\alpha_2$ phase and the $\gamma$ phase were observed. The white arrow shows the area of discontinuous precipitation in GBs. The $\beta_o$ phase also occurs in alloy 3Mo (**b**), alloy 5Mo (**c**), and alloy 7Mo (**d**) in addition to the $\gamma$ and $\alpha_2$ phases. Reprinted with permission from Ref. [111]. Copyright 2022 Elsevier.

H. Guo et al. [124] studied the thermal conductivity and phase morphology of Mg-RE (Rare-Earth) alloys (Mg–Nd, Mg–La, Mg–Sm, Mg–Ce) in both as-cast and annealed states. Nd and Sm have observable solid solubility in α-Mg. The addition of Nd and Sm reduces thermal conductivity. This effect was significantly stronger than after the addition of La and Ce. In turn, La and Ce have negligible solid solubility in an α-Mg matrix. La and Ce form the layers of intermetallic phases, which completely wet the Mg/Mg GBs (see Figure 21). GB wetting by the intermetallic Mg–RE phases was also observed in Mg–2Nd–4Zn [126], Mg–5Sn–2Zn–0.5Zr (wt%) [128], Mg–2Dy–0.5Zn (wt%) [129], Mg–14Li–0.5Ni alloys [130] and AZ31/ZK60 bimetal rods [131].

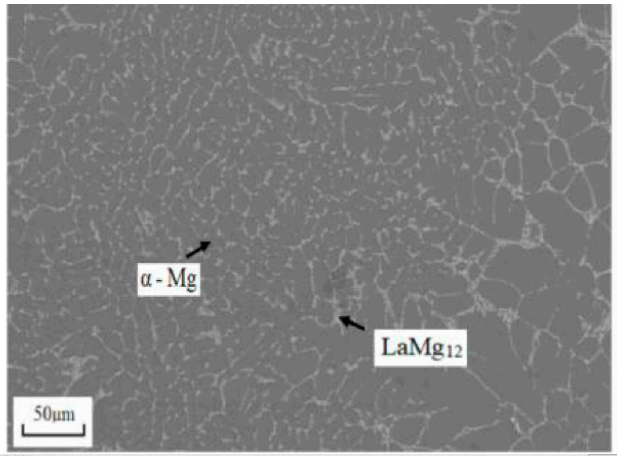

**Figure 21.** SEM-BSE micrograph of the Mg–4 wt% La alloy annealed at 400 °C [124].

GB wetting by a second solid phase was observed in multicomponent high-entropy alloys (HEA) such as in arc-melted $CoFeNi_{0.5}AlCr_x$ ($x$ = 0.25, 0.50, 0.75 and 1.00) alloy heat treated at 1200 °C [84], $CoCrFeNi(SiC)_x$ alloy deposited powder plasma arc additive manufacturing [132], in $Al_{0.2}MoNbTaTiW/MC$ refractory HEA composite manufactured by spark plasma sintering and hot extrusion [134], carbon-alloyed FeMnCr-$NiCo_{0.95}C_{0.05}$ HEA subjected to different thermal-mechanical treatments [136], AlCoCrFeNiTi-C HEA annealed at 1200 °C [138], NiCoCrAlY coating on 304 stainless steel laser processed at 950 °C [139], spark plasma sintered (SPS) HfNbTaTiZr HEA [140], AlCoCrCuFeNi HEA heat treated at 1200 °C [141], AlCoCrFeNiCu HEA coating deposited by the high velocity oxygen fuel spraying (HVOF) and vacuum heat treatment (VHT) at different temperatures (500, 700, 900 and 1100 °C) [142], $AlNb_2TiV$ low-weight refractory HEA [143] ans $Al_{10}Co_{19}Cr_{16}Fe_{20}Ni_{35}$ HEA homogenized at 1200 °C and annealed at 800 °C and at 590 °C [144].

## 7. Conclusions

In this review, several grain boundary (GB) wetting phenomena were analyzed. Especially important are the cases when the GB wetting phase is not liquid but solid. It turns out that in this case, the transition from partial to complete GB wetting can occur not only with increasing but also with decreasing temperature. Moreover, the portion of GBs fully covered by a layer of another solid phase can non-monotonously change with changing temperature. In this case, the wetting can be followed by dewetting. Afterward, the wetting appears again. The completely wetted GBs are substituted by continuous layers of a second solid phase. Differently, the completely wetted grain boundary triple junctions (TJ) are substituted with a trigonal prism of a wetting phase. As a result, the thermodynamic conditions for complete wetting of a GB TJ are less strong in comparison with a similar condition for GBs. In turn, this feature leads to the fact that TJs become fully wetted earlier (i.e., at lower temperatures) than GBs. In addition, they become dewetted later (i.e., at higher temperatures) than GBs. All this variety of GB and TJ wetting phenomena, in the hands of materials engineers, gives them a new instrument to tailor the properties of a broad spectrum of two and multiphase materials.

**Author Contributions:** Conceptualization, B.S. and A.K.; methodology, T.L.; formal analysis, A.K.; writing—original draft preparation, G.G.; writing—review and editing, B.S.; supervision, O.K.; project administration, O.K.; funding acquisition, A.G. All authors have read and agreed to the published version of the manuscript.

**Funding:** This research was funded by Russian Science Foundation, grant number 22-22-00511, https://rscf.ru/project/22-22-00511/ (accessed on 1 January 2023).

**Data Availability Statement:** Data are contained within the article.

**Acknowledgments:** Authors thank L.N. Shchur, E. Konstantinova, and D. Kagramanian for fruitful discussions.

**Conflicts of Interest:** The authors declare no conflict of interest. The funders had no role in the design of the study; in the collection, analyses, or interpretation of data; in the writing of the manuscript, or in the decision to publish the results.

## References

1. Jones, W.D. *Fundamental Principles of Powder Metallurgy*; Edward Arnold Ltd.: London, UK, 1960.
2. Protasova, S.G.; Kogtenkova, O.A.; Straumal, B.B.; Zięba, P.; Baretzky, B. Inversed solid-phase grain boundary wetting in the Al–Zn system. *J. Mater. Sci.* **2011**, *46*, 4349–4353. [CrossRef]
3. Cahn, J.W. Critical point wetting. *J. Chem. Phys.* **1977**, *66*, 3667–3676. [CrossRef]
4. Ebner, C.; Saam, W.F. New phase-transition phenomena in thin argon films. *Phys. Rev. Lett.* **1977**, *38*, 1486–1489. [CrossRef]
5. Bonn, D.; Eggers, J.; Indekeu, J.; Meunier, J.; Rolley, E. Wetting and spreading. *Rev. Mod. Phys.* **2009**, *81*, 739–805. [CrossRef]
6. Tang, M.; Carter, W.C.; Cannon, R.M. Diffuse interface model for structural transitions of grain boundaries. *Phys. Rev. B* **2006**, *73*, 024102. [CrossRef]
7. Luo, J.; Tang, M.; Cannon, R.M.; Carter, W.C.; Chiang, Y.M. Pressure-balance and diffuse-interface models for surficial amorphous films. *Mater. Sci. Eng. A* **2006**, *422*, 19–28. [CrossRef]
8. Kaplan, W.D.; Chatain, D.; Wynblatt, P.; Carter, W.C. A review of wetting versus adsorption, complexions, and related phenomena: The Rosetta stone of wetting. *J. Mater. Sci.* **2013**, *48*, 5681–5717. [CrossRef]

9. Straumal, B.B.; Polyakov, S.A.; Bischoff, E.; Gust, W.; Mittemeijer, E.J. Faceting of Σ3 and Σ9 grain boundaries in copper. *Interface Sci.* **2001**, *9*, 287–292. [CrossRef]
10. Luo, J. Stabilization of nanoscale quasi-liquid interfacial films in inorganic materials: A review and critical assessment. *Crit. Rev. Solid State Mater. Sci.* **2007**, *32*, 67–109. [CrossRef]
11. Straumal, B.B.; Baretzky, B. Grain boundary phase transitions and their influence on properties of polycrystals. *Interface Sci.* **2004**, *12*, 147–155. [CrossRef]
12. Eustathopoulos, N. Energetics of solid/liquid interfaces of metals and alloys. *Int. Met. Rev.* **1983**, *28*, 189–210. [CrossRef]
13. Straumal, B.B.; Gornakova, A.S.; Kogtenkova, O.A.; Protasova, S.G.; Sursaeva, V.G.; Baretzky, B. Continuous and discontinuous grain boundary wetting in the Zn–Al system. *Phys. Rev. B* **2008**, *78*, 054202. [CrossRef]
14. Straumal, B.; Gust, W.; Watanabe, T. Tie lines of the grain boundary wetting phase transition in the Zn-rich part of the Zn–Sn phase diagram. *Mater. Sci. Forum* **1999**, *294–296*, 411–414. [CrossRef]
15. Straumal, B.; Muschik, T.; Gust, W.; Predel, B. The wetting transition in high and low energy grain boundaries in the Cu(In) system. *Acta Metall. Mater.* **1992**, *40*, 939–945. [CrossRef]
16. Straumal, B.; Molodov, D.; Gust, W. Wetting transition on the grain boundaries in Al contacting with Sn-rich melt. *Interface Sci.* **1995**, *3*, 127–132. [CrossRef]
17. López, G.A.; Mittemeijer, E.J.; Straumal, B.B. Grain boundary wetting by a solid phase; microstructural development in a Zn–5 wt.% Al alloy. *Acta Mater.* **2004**, *52*, 4537–4545. [CrossRef]
18. Qin, S.S.; Bendo, A.; Tsuchiya, T.; Lee, S.; Matsuda, K. Effect of cooling rate on precipitation during homogenization cooling in excess Si type Al-Mg-Si alloy. *Mater. Lett.* **2020**, *278*, 128363. [CrossRef]
19. Kogtenkova, O.A.; Zieba, P.; Czeppe, T.; Litynska-Dobrzynska, L.; Straumal, B.B.; Nekrasov, A.N. Wetting of grain boundaries by the second solid phase in the Al-based alloys. *Bull. Russ. Acad. Sci. Phys.* **2013**, *77*, 1386–1390. [CrossRef]
20. Tian, Y.B.; Shen, J.Q.; Hu, S.S.; Han, J.; Wang, Q.; Cai, Y.C. Effects of ultrasonic peening treatment layer by layer on microstructure of components fabricated by wire and arc additive manufacturing. *Mater. Lett.* **2021**, *284*, 128917. [CrossRef]
21. Straumal, B.B.; Baretzky, B.; Kogtenkova, O.A.; Straumal, A.B.; Sidorenko, A.S. Wetting of grain boundaries in Al by the solid $Al_3Mg_2$ phase. *J. Mater. Sci.* **2010**, *45*, 2057–2061. [CrossRef]
22. Gao, T.; Bian, Y.; Liu, L.; Zhao, K.; Hu, K.; Liu, X. Modification of primary and eutectic phases in Al-33.2Cu and Al-20$Mg_2$Si alloys by nano-treating. *Mater. Lett.* **2021**, *286*, 129218. [CrossRef]
23. Liu, T.Y.; Chen, S.Y.; Wang, S.; Wang, L.Z.; Sun, J.B.; Jiang, Y.F. Effect of annealing on the structure and magnetic properties of $SmCo_5$-based ribbons with Al-Cu-Fe addition. *Mater. Lett.* **2021**, *286*, 129237. [CrossRef]
24. Kogtenkova, O.A.; Straumal, B.B.; Protasova, S.G.; Gornakova, A.S.; Zięba, P.; Czeppe, T. Effect of the wetting of grain boundaries on the formation of a solid solution in the Al–Zn system. *JETP Lett.* **2012**, *96*, 380–384. [CrossRef]
25. Duan, S.W.; Guo, F.Q.; Qin, S.S.; Gao, Y.; Matsuda, K.; Zou, Y. Effects of cooling rates on precipitates in homogenized Al-Cu-Li alloy. *Mater. Lett.* **2021**, *293*, 129695. [CrossRef]
26. Wang, X.Y.; Jiang, J.T.; Li, G.; Shao, W.Z.; Zhen, L. Precipitation during quenching in 2A97 aluminum alloy and the influences from grain structure. *Materials* **2021**, *11*, 2802. [CrossRef]
27. Mao, G.L.; Tong, G.Z.; Gao, W.L.; Liu, S.G.; Zhong, L.W. The poisoning effect of Sc or Zr in grain refinement of Al-Si-Mg alloy with Al-Ti-B. *Mater. Lett.* **2021**, *302*, 130428. [CrossRef]
28. Ke, B.; Ye, L.Y.; Zhang, Y.; Liu, X.D.; Dong, Y.; Wang, P.; Tang, J.G.; Liu, S.D. Enhanced strength and electrical conductivities of an Al-Zn-Mg aluminum alloy through a new aging process. *Mater. Lett.* **2021**, *304*, 30586. [CrossRef]
29. Gao, T.; Liu, L.Y.; Liu, S.S.; Yuan, C.H.; Bian, Y.H.; Liu, X.F. The growth behavior of Al2Cu phase in confined spaces constituted by gamma-$Al_2O_3$ particle clusters. *Mater. Lett.* **2021**, *304*, 130711. [CrossRef]
30. Pouraliakbar, H.; Beygi, R.; Fallah, V.; Monazzah, A.H.; Jandaghi, M.R.; Khalaj, G.; da Silva, L.F.M.; Pavese, M. Processing of Al-Cu-Mg alloy by FSSP: Parametric analysis and the effect of cooling environment on microstructure evolution. *Mater. Lett.* **2022**, *308*, 131157. [CrossRef]
31. Yu, X.; Chen, S.Y.; Gu, F.; Zhang, Z.Y.; Sun, J.B.; Cui, C.X. Preparation of Alnico magnet with high magnetization by thermal deformation. *Mater. Lett.* **2022**, *310*, 131503. [CrossRef]
32. Wang, G.; Gu, Z.; Yu, G. Precipitates evolution of the AA7075-H18 alloy sheet during the application of the solution heat treatment process. *Mater. Lett.* **2022**, *318*, 132230. [CrossRef]
33. Que, Z.; Wang, Y.; Fan, Z.; Hashimoto, T.; Zho, X. Enhanced heterogeneous nucleation of $Al_6$(Fe,Mn) compound in Al alloys by interfacial segregation of Mn on $TiB_2$ particles surface. *Mater. Lett.* **2022**, *323*, 132570. [CrossRef]
34. Rogachev, S.O.; Belov, N.A.; Cherkasov, S.O.; Sundeev, R.V. Joint effect of electromagnetic casting and high-pressure torsion on the structure and hardening of $Al_{3.3}Cu_{2.5}Mn_{0.5}Zr$ (wt.%) alloy. *Mater. Lett.* **2022**, *324*, 132776. [CrossRef]
35. Song, Z.; Niu, R.; Cui, X.; Bobruk, E.V.; Murashkin, Y.M.; Enikeev, N.A.; Gu, J.; Song, M.; Bhatia, V.; Ringer, S.P.; et al. Mechanism of room-temperature superplasticity in ultrafine-grained Al–Zn alloys. *Acta Mater.* **2023**, *246*, 118671. [CrossRef]
36. Kul, M.; Danaci, I.; Gezer, S.; Karaca, B. Effect of boronizing composition on hardness of boronized AISI 1045 steel. *Mater. Lett.* **2020**, *279*, 128510. [CrossRef]
37. Straumal, B.B.; Kucheev, Y.O.; Efron, L.I.; Petelin, A.L.; Dutta Majumdar, J.; Manna, I. Complete and incomplete wetting of ferrite grain boundaries by austenite in the low-alloyed ferritic steel. *J. Mater. Eng. Perform.* **2012**, *21*, 667–670. [CrossRef]

38. Tu, X.X.; Xiao, L.R.; Zhao, X.J.; Cai, Z.Y.; Peng, Z.W.; Wei, D.M. Effects of thermal-cold cycling on the dimensional stability of TiC reinforced steel matrix composite. *Mater. Lett.* **2020**, *279*, 128483. [CrossRef]
39. Li, J.S.; Qin, W.B.; Peng, P.; Chen, M.; Mao, Q.Z.; Yue, W.; Kang, J.J.; Meng, D.Z.; She, D.S.; Zhu, X.B. Effects of geometric dimension and grain size on impact properties of 316L stainless steel. *Mater. Lett.* **2021**, *284*, 128908. [CrossRef]
40. Wei, T.; Ding, K.; Wu, G.Z.; Liu, X.; Fan, M.J.; Zhang, Y.B.; He, Y.; Huo, X.; Gao, Y.L. Stress rupture initiated by the carbides in the grain boundaries of the multi-pass weld metal. *JMR&T* **2021**, *10*, 282–290. [CrossRef]
41. Rong, X.Q.; Guo, H.; Enomoto, M.; Shang, C.J. Enhancement of Cu nano-precipitation by Al addition in a Cu-Ni bearing low alloy steel. *Mater. Lett.* **2021**, *284*, 128938. [CrossRef]
42. Wang, H.; Wang, T. A comparative study of high boron alloys with 2.0 wt% B based on 304 and 316 stainless steels. *Mater. Lett.* **2021**, *285*, 129035. [CrossRef]
43. Xu, S.; Shu, X.D.; Li, S.X.; Chen, J. Flow stress curve modification and constitutive model of 20CrMoA steel during warm deformation. *Metals* **2020**, *10*, 1602. [CrossRef]
44. Min, W.; Guoping, L.; Lixin, W.; Lifeng, H.; Yinghui, W. Temperature dependence of precipitation mechanism of intragranular $\chi$ phase in super duplex stainless steel S32750. *Mater. Lett.* **2021**, *287*, 29304. [CrossRef]
45. Zou, J.; Lu, L.; Kolisnichenko, O.V.; Chen, W.; Yu, J.M. Gas nitriding of a plasma detonation modified die steel. *Mater. Lett.* **2021**, *287*, 129297. [CrossRef]
46. Han, K.; Smith, G.D.W.; Edmonds, D.V. Pearlite phase transformation in Si and V steel. *Metall. Mater. Trans. A* **1995**, *26*, 1617–1631. [CrossRef]
47. Zhang, H.Y.; Li, Y.M.; Liang, W.; Zheng, L.W. Observation of hydrogen diffusion channel and hydrogen trap in 304 austenitic stainless steel. *Mater. Lett.* **2021**, *290*, 129453. [CrossRef]
48. Han, G.; Shang, C.J.; Xie, Z.J.; Misra, R.D.K.; Wang, J.L. On the thermal and mechanical stability of reverted austenite by intercritical tempering. *Mater. Lett.* **2021**, *291*, 129457. [CrossRef]
49. Saha, A.; Mondal, D.K.; Biswas, K.; Maity, J. Development of high strength ductile hypereutectoid steel by cyclic heat treatment process. *Mater. Sci. Eng. A* **2012**, *541*, 204–215. [CrossRef]
50. Zhao, F.; Hu, H.; Liu, X.; Zhang, Z.; Xie, J. Effect of billet microstructure and deformation on austenite grain growth in forging heating of a medium-carbon microalloyed steel. *J. All. Compd.* **2021**, *869*, 159326. [CrossRef]
51. Zhang, D.Q.; Liu, G.; Sun, X.J. Different roles of reversed austenite, athermal martensite and tempered martensite on low-temperature toughness in ultra-low carbon medium Mn steel. *Mater. Lett.* **2021**, *297*, 129958. [CrossRef]
52. Li, X.K.; Wang, R.; Xin, Z.; Dong, Y.J.; Xu, J.H.; Wei, D.Q. Changes in surface roughness and microstructure of 45 steel after irradiation by electron beam. *Mater. Lett.* **2021**, *296*, 129934. [CrossRef]
53. Wang, L.; Cheng, X.Y.; Peng, H.; Zhao, P.W.; Cai, Z.X. Effect of tempering temperature on hydrogen embrittlement in V-containing low alloy high strength steel. *Mater. Lett.* **2021**, *302*, 130327. [CrossRef]
54. Li, T.L.; Yan, S.; Liu, X.H. Enhancement austenite content in medium-Mn steel by introducing cold-rolled deformation and inhibiting subsequent recrystallization. *Mater. Lett.* **2021**, *301*, 130249. [CrossRef]
55. Ni, X.Q.; Kong, D.C.; Wu, W.H.; Zhang, L.; Dong, C.F. Deformation-induced martensitic transformation in 316L stainless steels fabricated by laser powder bed fusion. *Mater. Lett.* **2021**, *302*, 130377. [CrossRef]
56. Han, K.; Mottishaw, T.D.; Smith, G.D.W.; Edmonds, D.V. Effects of vanadium addition on nucleation and growth of pearlite in high carbon steel. *Mater. Sci. Technol.* **1994**, *10*, 955–963. [CrossRef]
57. Yuan, J.; Xiao, Y.; Min, N.; Li, W.; Zhao, S. The influence of precipitate morphology on the growth of austenite grain in Nb-Ti-Al microalloyed steels. *Materials* **2022**, *15*, 3176. [CrossRef]
58. Zielinski, A.; Wersta, R.; Sroka, M. The study of the evolution of the microstructure and creep properties of Super 304H austenitic stainless steel after aging for up to 50,000 h. *Arch. Civil Mech. Eng.* **2022**, *22*, 89. [CrossRef]
59. Wang, B.X.; Zhang, Y.; Qiu, F.; Cai, G.S.; Cui, W.W.; Hu, Z.R.; Zhang, H.; Tyrer, N.; Barber, G.C. Role of trace nanoparticles in manipulating the widmanstatten structure of low carbon steel. *Mater. Lett.* **2021**, *306*, 130853. [CrossRef]
60. Huang, S.; Yu, Y.S.; Wang, Z.Q.; Su, S.; Chen, K.; Yuan, S.F.; Xie, Z.J.; Shang, C.J. Crystallographic insights into the role of nickel on hardenability of wear-resistant steels. *Mater. Lett.* **2021**, *306*, 130961. [CrossRef]
61. Krugljakow, A.A.; Rogachev, S.O.; Lebedeva, N.V.; Sokolov, P.Y.; Arsenkin, A.M.; Khatkevich, V.M. On the nature of hot work hardening phenomenon in die steel with regulated austenitic transformation during exploitation. *Mater. Sci. Eng. A* **2022**, *833*, 142548. [CrossRef]
62. Kaushik, N.C.; Maitra, A.; Ajay Vamsi, J.; Sai Krishna, T.; Tarun Saty, A. Understanding elastic/plastic nature of phases in Fe–13Cr–1C hardfaced coating through accelerated property mapping technique. *Mater. Lett.* **2022**, *320*, 132335. [CrossRef]
63. Wang, X.L.; Xie, Z.J.; Wang, Z.Q.; Yu, Y.S.; Wu, L.Q.; Shang, C.J. Crystallographic study on microstructure and impact toughness of coarse grained heat affected zone of ultra-high strength steel. *Mater. Lett.* **2022**, *323*, 132552. [CrossRef]
64. Liu, Z.; Yang, J.; Guo, H.; Wang, X.; Shang, C. Crystallographic study on deformed bainite structure of ultra-high strength steel and its relationship with strength and ductile-brittle transition temperature. *Mater. Lett.* **2022**, *326*, 132947. [CrossRef]
65. Wang, J.; Qian, R.; Yang, X.; Zhong, Y.; Shang, C. Effect of segregation on the microstructure and properties of a quenching and partitioning steel. *Mater. Lett.* **2022**, *325*, 132815. [CrossRef]
66. Dlouhý, J.; Chvostová, E.; Nový, Z. Boron influence on the development of Laves phase in 10Cr creep resistant steel. *Mater. Lett.* **2022**, *327*, 132918. [CrossRef]

67. Zhang, Y.; Huo, W.; Song, R.; Wang, L.; Geng, Z.; Wang, J.; Zhou, T.; Xue, H. The effect of isothermal bainitic transformation time on austenite stability of TRIP-980 steel with high ductility. *Mater. Lett.* **2022**, *326*, 132927. [CrossRef]
68. Yu, H.; Yu, Y.; Wang, Z.; Li, F.; Hu, B.; Liu, S. On the variant pairing in transformation product of high strength low alloy steel depending on cooling rate. *Mater. Lett.* **2022**, *326*, 132953. [CrossRef]
69. Milyutin, V.A.; Bureš, R.; Fáberová, M.; Molčanová, Z.; Csanádi, T. Structure, magnetostriction and elastic properties of an $Fe_3Ga_{0.7}Cu_{0.3}$ alloy. *Mater. Lett.* **2022**, *327*, 133063. [CrossRef]
70. Li, X.L.; Li, H.Z.; Liu, L.X.; Deng, X.T.; Wang, Z.D. The formation mechanism of complex carbides in Nb-V microalloyed steel. *Mater. Lett.* **2022**, *311*, 131544. [CrossRef]
71. Li, S.; Ma, J.; Wang, J.; Fan, G.; Li, H.; Jiang, Z.; Han, P.; Liang, W. Impact of boron addition on the hot deformation behavior and microstructure evolution of S31254. *Mater. Lett.* **2022**, *315*, 131971. [CrossRef]
72. Wang, R.; Huang, Y.; Wei, D.; Luo, J.; Ren, X.; Li, X.; Lu, J.; Sui, X. Scanning electron beam surface strengthening of column-faced 45 steel. *Mater. Lett.* **2022**, *324*, 132497. [CrossRef]
73. Xie, Z.J.; Li, Q.; Liu, Z.P.; Zhou, W.H.; Wang, X.L.; Yu, Q.; Xiao, D.H.; Shang, C.J. Enhanced ductility and toughness by tailoring heterogenous microstructure in an ultra-heavy gauge high strength steel with severe centerline segregation. *Mater. Lett.* **2022**, *323*, 132525. [CrossRef]
74. Wang, M.; Luo, Z.; Yang, J.; Xie, G.; Liu, Z. Diffusion behavior and formation mechanism of compounds in titanium-steel bonding process at high temperature. *Mater. Lett.* **2023**, *330*, 133309. [CrossRef]
75. He, Y.H.; Liu, J.; Zhang, S.Q.; Li, Y.Y.; Gao, X. Effect of heat treatment on the microstructure and corrosion resistance of 316L stainless steel fabricated by hybrid in-situ rolled wire-arc additive manufacturing. *Mater. Lett.* **2023**, *331*, 133398. [CrossRef]
76. Zheng, C.L.; Zhang, Y.P.; Li, S.Y.; Zhang, P.J.; Yu, J.K.; Zhang, F.C. In-situ generation process and properties of nanocrystalline layer in bainitic steel surface during rolling contact. *Mater. Lett.* **2023**, *333*, 133633. [CrossRef]
77. Straumal, B.B.; Kogtenkova, O.A.; Straumal, A.B.; Kuchyeyev, Y.O.; Baretzky, B. Contact angles by the solid-phase grain boundary wetting in the Co–Cu system. *J. Mater. Sci.* **2010**, *45*, 4271–4275. [CrossRef]
78. Zhang, Y.L.; Jiang, X.S.; Fang, Y.J.; Sun, H.L.; Song, T.F.; Mo, D.F.; Li, X.; Luo, Z.P. Vacuum diffusion bonding of CoCrFeNiMo MEAs and Inconel 718 using Ni interlayer. *Mater. Lett.* **2020**, *279*, 128509. [CrossRef]
79. Kanetas, P.J.P.; Calvo, J.; Rodriguez-Calvillo, P.; Marrero, J.M.C.; Antunano, M.A.Z.; Guerrero-Mata, M.P. EBSD Study of delta-processed Ni-based superalloy. *Metals* **2020**, *10*, 1466. [CrossRef]
80. Thulasiram, R.; Mani, S.; Ramaswamy, N.; Murugesan, M. Grain size refinement, texture analysis and effect on the tensile properties of a novel Inconel 718. *Mater. Lett.* **2021**, *292*, 129633. [CrossRef]
81. Yan, D.C.; Qiu, N.S.; Zuo, X.W. On the Cr-rich continuous and discontinuous precipitation kinetics in Ni-Cr alloys by microstructural characterization and differential scanning calorimetry analysis. *Mater. Lett.* **2021**, *296*, 129887. [CrossRef]
82. Wu, Y.; Li, Y.T.; Xu, Y.T.; Kang, M.D.; Wang, J.; Sun, B.D. Unveiling the precipitation-induced high-temperature oxidation behavior in a Ni-Al-Y alloy. *Mater. Lett.* **2021**, *297*, 129977. [CrossRef]
83. Babalola, B.J.; Ayodele, O.O.; Awotunde, M.A.; Akinwamide, S.O.; Olubambi, P.A. Microstructure and mechanical properties of Ni-17Cr-xCo ternary alloys fabricated via field-assisted sintering. *Mater. Lett.* **2021**, *302*, 130404. [CrossRef]
84. Quintana-Nedelcos, A.; Anis, M.; Osman, R.; Yang, J.; Leong, Z.; Azakli, Y.; Morley, N.A. On the structural, microstructural and magnetic properties evolution of $Ni_{0.5}$FeCoAlCrx alloys. *Mater. Lett.* **2022**, *311*, 131542. [CrossRef]
85. Tong, Y.X.; Liu, J.X.; Sun, S.B.; Chen, F.; Zarinejad, M. Unusual precipitation and its hardness enhancement in Fe-alloyed 60NiTi alloy. *Mater. Lett.* **2022**, *329*, 133170. [CrossRef]
86. Sun, Y.; Song, C.; Zhang, Y.; Li, M.; Zhang, Y. Oxidation on the current-carrying rolling surface and its subsequent impact on the damage of Cu contact pairs in $O_2/N_2$ mixture. *Mater. Lett.* **2021**, *288*, 129349. [CrossRef]
87. Straumal, B.; Kogtenkova, O.; Bulatov, M.; Nekrasov, A.; Baranchikov, A.; Baretzky, B.; Straumal, A. Wetting of grain boundary triple junctions by intermetallic Delta-phase in the Cu–In alloys. *J. Mater. Sci.* **2021**, *58*, 7840–7848. [CrossRef]
88. Nie, Q.; Wang, B.; Zhang, J.; Tang, W. Fabrication of the Ag-coated Invar/Cu bimetal matrix composites through spark plasma sintering: An investigation on microstructure and properties. *Mater. Lett.* **2022**, *321*, 132440. [CrossRef]
89. Straumal, B.B.; Kogtenkova, O.A.; Kolesnikova, K.I.; Straumal, A.B.; Bulatov, M.F.; Nekrasov, A.N. Reversible "wetting" of grain boundaries by the second solid phase in the Cu–In system. *JETP Lett.* **2014**, *100*, 535–539. [CrossRef]
90. Liang, S.L.; Wang, Y.H.; Wang, H.; Wang, J.; Jiang, S.H. Achieving improved strength and ductility through multi-pass cold deformation and annealing of a Cu-Zn-Bi alloy. *Mater. Lett.* **2023**, *330*, 133373. [CrossRef]
91. Dash, K.; Dash, A. In-situ formation of 2D-$TiC_x$ in Cu-$Ti_2$AlC composites: An interface reaction study. *Mater. Lett.* **2021**, *284*, 128935. [CrossRef]
92. Straumal, B.B.; Gornakova, A.S.; Prokofjev, S.I.; Afonikova, N.S.; Baretzky, B.; Nekrasov, A.N.; Kolesnikova, K.I. Continuous and discontinuous $\alpha$Ti layers between grains of $\beta$(Ti,Co) phase. *J. Mater. Eng. Perform.* **2014**, *23*, 1580–1584. [CrossRef]
93. Li, Z.; Luo, L.; Su, Y.; Luo, L.; Wang, B.; Wang, L.; Yao, M.; Guo, J.; Fu, H. In-situ investigation of $\beta/\alpha$ transformation in $\beta$-solidifying $\gamma$-TiAl alloys at different cooling rates. *Mater. Lett.* **2021**, *285*, 129092. [CrossRef]
94. Gornakova, A.S.; Prokofiev, S.I.; Kolesnikova, K.I.; Straumal, B.B. Formation regularities of grain boundary interlayers of the $\alpha$-Ti phase in binary titanium alloys. *Russ. J. Non-Ferr. Met.* **2016**, *57*, 229–235. [CrossRef]
95. Jiang, X.J.; Bai, J.; Yang, N.; Ran, Q.X.; Wang, S.Q. Effect of deformation on $\alpha$-$\beta$ phase transformation temperature of a metastable TiZr based alloy. *Mater. Lett.* **2021**, *285*, 129003. [CrossRef]

96. Gornakova, A.S.; Prokofiev, S.I.; Straumal, B.B.; Kolesnikova, K.I. Growth of (αTi) grain boundary layers in Ti–Co alloys. *Russ. J. Non-Ferr. Met.* **2016**, *57*, 703–709. [CrossRef]
97. Bi, Y.B.; Xu, Y.; Zhang, Y.; Xue, R.L.; Bao, Y. Single-pass laser welding of TC4 Ti alloy to 304 SS with V interlayer and V/Cu bilayer. *Mater. Lett.* **2021**, *285*, 129072. [CrossRef]
98. Gornakova, A.S.; Straumal, B.B.; Nekrasov, A.N.; Kilmametov, A.; Afonikova, N.S. Grain boundary wetting by a second solid phase in Ti–Fe alloys. *J. Mater. Eng. Perform.* **2018**, *27*, 4989–4992. [CrossRef]
99. Chen, X.; Huang, L.; Jiao, Y.; Wang, S.; An, Q.; Bao, Y.; Geng, L. Mechanisms of oxidation anisotropy between α-Ti (0001) and crystallographic planes in titanium matrix composites. *Mater. Lett.* **2021**, *286*, 129230. [CrossRef]
100. Ongwen, N.; Chanbi, D.; Ogam, E.; Odhiambo, H.; Fellah, Z.E.A. Microtructural and elastic properties of stable aluminium-rich TiAl and TiAl$_2$ formed phase intermetallics. *Mater. Lett.* **2021**, *287*, 129295. [CrossRef]
101. Zhang, S.Y.; Wang, Y.F.; Suo, T.; Yao, J.; Lin, X.; Huang, W.D.; Li, Y.L.; Shen, J.H. The effect of heat treatment on dynamic properties of an additively manufactured Ti-6Al-4V alloy. *Crystals* **2021**, *11*, 111. [CrossRef]
102. Zhang, L.; Zhao, Z.; Bai, P.; Du, W. EBSD investigation on microstructure evolution of in-situ synthesized TiC/Ti6Al4V composite coating. *Mater. Lett.* **2021**, *290*, 129449. [CrossRef]
103. Bazhina, A.D.; Bazhin, P.M.; Chizhikov, A.P.; Konstantinov, S.; Stolin, A.M. Influence of high-temperature annealing on structure of titanium aluminide materials obtained by combustion and high-temperature shear deformation. *Intermetallics* **2021**, *139*, 107313. [CrossRef]
104. Ma, W.; Wang, F.; Chen, B.H.; Li, B.; Zhang, X.Y.; Ma, M.Z.; Liu, R.P. Thermal compression behavior and microstructural evolution of Ti-30-5-3 alloys in lower alpha plus beta region. *Mater. Lett.* **2021**, *297*, 129876. [CrossRef]
105. Paghandeh, M.; Zarei-Hanzaki, A.; Abedi, H.R.; Vahidshad, Y. The enhanced warm temperature ductility of Ti-6Al-4V alloy through strain induced martensite reversion and recrystallization. *Mater. Lett.* **2021**, *302*, 130405. [CrossRef]
106. Chookajorn, T.; Murdoch, H.A.; Schuh, C.A. Design of stable nanocrystalline alloys. *Science* **2012**, *337*, 951–954. [CrossRef] [PubMed]
107. Gao, Q.; Jiang, X.S.; Sun, H.L.; Song, T.F.; Mo, D.F.; Li, X. Interfacial reaction and microstructure investigation of 4J36/Ni/Cu/V/TC4 diffusion-bonded joints. *Mater. Lett.* **2021**, *305*, 130809. [CrossRef]
108. Gao, Y.D.; Zhang, Y.; Xu, Y.; Zhou, J.P. The butt of CP-Ti/304 stainless steel and CP-Ti/T2 bimetallic sheets using laser-induction heating welding technology. *Mater. Lett.* **2021**, *307*, 131054. [CrossRef]
109. Su, G.; Yun, Z.; Lin, Y.C.; He, D.G.; Zhang, S.; Chen, Z.J. Microstructure evolution and a unified constitutive model of Ti-55511 alloy compressed at stepped strain rates. *Materials* **2021**, *14*, 6750. [CrossRef]
110. Wang, Y.C.; Xue, X.Y.; Kou, H.C.; Chang, J.X.; Yin, Z.W.; Li, J.S. Improvement of microstructure homogenous and tensile properties of powder hot isostatic pressed TA15 titanium alloy via heat treatment. *Mater. Lett.* **2022**, *311*, 131585. [CrossRef]
111. Musi, M.; Clemens, H.; Stark, A.; Staron, P.; Spoerk-Erdely, P. Phase transformations and phase stability in the Ti-44 at.%Al-(0-7 at.%) Mo system. *Intermetallics* **2022**, *143*, 107484. [CrossRef]
112. Lin, T.; Song, K.; Shao, H.; Lu, H. Effect of Nb content on Ti-Mo-Nb alloy materials for neutron high pressure diffraction. *Mater. Lett.* **2022**, *314*, 131821. [CrossRef]
113. Tang, H.; Liu, Y.; Zhao, D.; Song, M. Achieving high strength and large ductility via Zr-rich stripes in Ti-15Zr alloy. *Mater. Lett.* **2022**, *318*, 132194. [CrossRef]
114. Gao, Q.; Jiang, X.; Sun, H.; Zhang, Y.; Fang, Y.; Mo, D.; Li, X. Performance and microstructure of TC4/Nb/Cu/316L welded joints subjected to cryogenic treatment. *Mater. Lett.* **2022**, *321*, 132453. [CrossRef]
115. Nigito, E.; Diemer, F.; Husson, S.; Ou, S.F.; Tsai, M.H.; Rézaï-Aria, F. Microstructure of NiTi superelastic alloy manufactured by selective laser melting. *Mater. Lett.* **2022**, *324*, 132665. [CrossRef]
116. Xiao, C.; Zhang, H.; Davoodi, D.; Miri, R.; Tayebi, M. Microstructure evolutions of Ti-Al-Nb alloys with different Ta addition, produced by mechanical alloying and spark plasma sintering. *Mater. Lett.* **2022**, *323*, 132568. [CrossRef]
117. Wei, J.; Yang, F.; Qi, M.; Sui, Y.; Chen, C.; Guo, Z. Propagation mechanism of crack in adiabatic shear band of PM Ti-6Al-4V during hot deformation. *Mater. Lett.* **2022**, *324*, 132696. [CrossRef]
118. Xu, Y.; Liu, Z.; Zhu, X.; Jiang, Z.; Chen, H.; Wang, N. Effect of rare earth Ce addition on microstructure and mechanical properties of titanium alloy Ti-6Al-4V. *Mater. Lett.* **2023**, *330*, 133244. [CrossRef]
119. Li, J.; Sun, K.; Li, X.; Meng, X.; Cai, W. High damping performances over wide temperature range in the B doped Ti-Ni shape memory alloys. *Mater. Lett.* **2023**, *330*, 133245. [CrossRef]
120. Chen, X.F.; Tang, B.; Wei, B.B.; Zhang, X.; Li, J.S. Investigation on recrystallization behavior of Ti-47Al-1.5Re-X (Cr, Mn, V, Nb) alloy during hot deformation. *Mater. Lett.* **2023**, *331*, 33484. [CrossRef]
121. Cheng, F.; Wang, H.M.; Yang, J.W.; Li, Z.; Cheng, X.; Tian, X.J. Deformation kinking in duplex titanium alloy with widmannstatten laths under high strain rates. *Mater. Lett.* **2023**, *333*, 133591. [CrossRef]
122. Huang, G.Y.; Zhang, G.S.; Song, P.; Liu, X.M.; Lv, X.; Li, M.; Zhang, J.H.; Deng, W.K.; Guo, D.F. Tailoring pre-deformation microstructure-An easy way for nanocrystallization. *Mater. Lett.* **2022**, *308*, 131143. [CrossRef]
123. Straumal, B.B.; Gornakova, A.S.; Kucheev, Y.O.; Baretzky, B.; Nekrasov, A.N. Grain boundary wetting by a second solid phase in the Zr–Nb alloys. *J. Mater. Eng. Perform.* **2012**, *21*, 721–724. [CrossRef]
124. Guo, H.Y.; Liu, S.H.; Huang, L.; Wang, D.Q.; Du, Y.; Chu, M.Q. Thermal conductivity of as-cast and annealed Mg-RE binary alloys. *Metals* **2021**, *11*, 554. [CrossRef]

125. Straumal, A.B.; Mazilkin, I.A.; Tsoi, K.V.; Baretzky, B.; Straumal, B.B. "Wetting" phase transitions by the second solid phase for linear defects (grain boundary triple junctions). *JETP Lett.* **2020**, *112*, 257–261. [CrossRef]
126. Dong, N.N.; Sun, L.X.; Ma, H.B.; Jin, P.P. Effects of cryogenic treatment on microstructures and mechanical properties of Mg-2Nd-4Zn alloy. *Mater. Lett.* **2021**, *305*, 130699. [CrossRef]
127. Straumal, A.; Mazilkin, I.; Tzoy, K.; Straumal, B.; Bryła, K.; Baranchikov, A.; Eggeler, G. Bulk and surface low temperature phase transitions in the Mg-alloy EZ33A. *Metals* **2020**, *10*, 1127. [CrossRef]
128. Zhou, T.S.; Guo, F.F.; Zhang, Q.F.; Liu, D.X. Offsetting strength-ductility tradeoff in Mg-Sn-Zn-Zr alloy by a novel differential-thermal ECAP process. *Mater. Lett.* **2021**, *305*, 130764. [CrossRef]
129. Xiao, N.; Zeng, Y.Z.; Lu, X.L.; Sun, Y.H.; Sun, B.Z. On the $\gamma'$ and W strengthening precipitates in Dy and Zn microalloyed magnesium alloys. *Mater. Lett.* **2021**, *307*, 131028. [CrossRef]
130. Zhang, S.; Sun, B.; Wu, R.Z.; Zhou, Y.; Wu, Q. Nanocrystalline strengthened Mg-Li alloy with a bcc structure prepared via heat treatment and rolling. *Mater. Lett.* **2022**, *312*, 131680. [CrossRef]
131. Chang, L.L.; Su, X.J.; Qin, J.L. Uneven microstructure in ZK60 alloy as a core of AZ31/ZK60 composite rods. *Mater. Lett.* **2022**, *325*, 132666. [CrossRef]
132. Shen, Q.K.; Kong, X.D.; Chen, X.Z.; Yao, X.K.; Deev, V.B.; Prusov, E.S. Powder plasma arc additive manufactured CoCrFeNi(SiC)(x) high-entropy alloys: Microstructure and mechanical properties. *Mater. Lett.* **2021**, *282*, 128736. [CrossRef]
133. Straumal, B.B.; Korneva, A.; Kuzmin, A.; Lopez, G.; Rabkin, E.; Straumal, A.B.; Gerstein, G.; Gornakova, A.S. The grain boundary wetting phenomena in the Ti-containing high entropy alloys: A review. *Metals* **2021**, *11*, 1881. [CrossRef]
134. Han, J.S.; Su, B.; Zhang, A.J.; Meng, J.H.; Wu, Y.Z. Forming and characterization of $Al_{0.2}$MoNbTaTiW/MC refractory high-entropy alloy composite by spark plasma sintering and hot extrusion. *Mater. Lett.* **2021**, *284*, 128979. [CrossRef]
135. Straumal, B.B.; Korneva, A.; Lopez, G.A.; Kuzmin, A.; Rabkin, E.; Gerstein, G.; Straumal, A.B.; Gornakova, A.S. Grain boundary wetting by a second solid phase in the high entropy alloys: A review. *Materials* **2021**, *14*, 7506. [CrossRef]
136. Astafurova, E.; Melnikov, E.; Astafurov, S.; Reunova, K.; Panchenko, M.; Moskvina, V.; Tumbusova, I. A comparative study of a solid solution hardening in carbon-alloyed FeMnCrNiCo0.95C0.05 high-entropy alloy subjected to different thermal–mechanical treatments. *Mater. Lett.* **2021**, *285*, 129073. [CrossRef]
137. Straumal, B.; Rabkin, E.; Lopez, G.A.; Korneva, A.; Kuzmin, A.; Gornakova, A.S.; Valiev, R.Z.; Straumal, A.; Baretzky, B. Grain boundary wetting phenomena in the high entropy alloys containing nitrides, carbides, borides, silicides, and hydrogen: A review. *Crystals* **2021**, *11*, 1540. [CrossRef]
138. Sekhar, R.A.; Shifin, S.; Kumar, A.A.; Nair, A.H.; Sudhees, A.; Krishnan, J. AlCoCrFeNiTi-C alloy with TiC nano precipitates processed through mechanical alloying and spark plasma sintering. *Mater. Lett.* **2021**, *285*, 129185. [CrossRef]
139. Nie, J.H.; Li, Y.X.; Chen, B.W.; Yang, Y.X.; Zhang, H.J.; Liu, S.Y.; Wei, S.Z.; Cai, J.; Guan, Q.F. Evolution of oxide layer during high-temperature oxidation of NiCoCrAlY coating via laser cladding on 304 stainless steel. *Mater. Lett.* **2021**, *286*, 129233. [CrossRef]
140. Lukac, F.; Vilemova, M.; Klementova, M.; Minarik, P.; Chraska, T. The origin and the effect of the fcc phase in sintered HfNbTaTiZr. *Mater. Lett.* **2021**, *286*, 129224. [CrossRef]
141. Deng, N.; Wang, J.; Wang, J.X.; He, Y.X.; Beaugnon, E.; Li, J.S. Effect of high magnetic field assisted heat treatment on microstructure and properties of AlCoCrCuFeNi high-entropy alloy. *Mater. Lett.* **2021**, *303*, 130540. [CrossRef]
142. Zhou, Y.; Kang, J.; Zhang, J.; Fu, Z.; Zhu, L.; She, D. Effect of vacuum heat treatment on microstructure and mechanical properties of HVOF sprayed AlCoCrFeNiCu high-entropy alloy coating. *Mater. Lett.* **2022**, *323*, 132551. [CrossRef]
143. Zhu, X.P.; Gao, N.; Bai, Z.C.; Wang, K.; Yao, J.Q.; Fan, Z.T.; Wang, Z.D.; Liu, X.W. Phase stability of a light-weight AlNb2TiV refractory high-entropy alloy at high temperature. *Mater. Lett.* **2022**, *325*, 132897. [CrossRef]
144. Yen, S.; Liu, Y.; Chu, S.; Chang, C.; Lin, S.; Tsai, M.-H. B2-strengthened Al-Co-Cr-Fe-Ni high entropy alloy with high ductility. *Mater. Lett.* **2022**, *325*, 132828. [CrossRef]
145. Sursaeva, V.G.; Straumal, B.B.; Gornakova, A.S.; Shvindlerman, L.S.; Gottstein, G. Effect of faceting on grain boundary motion in Zn. *Acta Mater.* **2008**, *56*, 2728–2734. [CrossRef]